UNIVERSITÀ DI NAPOLI
"FEDERICO II"

Tesi di Dottorato di Ricerca in

Fisica Fondamentale ed Applicata

XIX ciclo

Sara Rombetto

Microwave Induced Resonant Quantum Phenomena in Josephson Devices

Dicembre 2006

Coordinatore: Prof. G. Miele
Candidato: S.Rombetto

to my parents

Tesi svolta in collaborazione con le seguenti istituzioni:

Istituto di Cibernetica "E. Caianiello" del CNR

Dr. Berardo Ruggiero - tutor

Seconda Università di Napoli

Prof. Paolo Silvestrini - tutor

Università degli Studi di Napoli "Federico II"

Prof. Arturo Tagliacozzo - tutor

Centre de Recherches sur les Très Basses Températures (CRTBT) - CNRS , Grenoble, France

Dr. Olivier Buisson

Landau Institute, Moscow, Russia

Prof. Yuri N. Ovchinnikov

Contents

Acknowledgments

I would like to thank all the people who supported me during my studies. Results I present in following chapters are the result of work that I did together with the Macroscopic Quantum Coherence group, other colleagues and thanks to international collaboration.

Throughout these years there have been many persons who have supported me, which require mention.

First and foremost, I wish to express my gratitude to my advisors, Dr.Berardo Ruggiero and Prof.Paolo Silvestrini, for their invaluable guide and suggestions they gave me during my researches. I am indebted with Prof.Arturo Tagliacozzo for his advice in improving this work.

I wish to thank also the other members of the MQC group: firstly Dr.Maurizio Russo and Dr.Carmine Granata, their hints have been fundamental for the work I present here. I have also benefited of useful discussions and friendly collaborations with Dr.Roberto Russo and Dott.ssa V.Corato. Moreover I would thank all the friends and colleagues at ICIB-CNR, and my special thanks go to Dott.ssa Emanuela Esposito, for useful discussions and for her great availability and experimental suggestions.

I would thank also Prof.Antonello Andreone and his group for supporting me during measurements in Naples.

I am grateful to the Director of ICIB-CNR, Prof.Settimo Termini for his hospitality in the Institute.

A special thank to Dr.Olivier Buisson, who dedicated much time discussing with me during my stage in Grenoble and helped me to discover the wonderful world of microwave. Moreover I would thank him for his hospitality in Grenoble.
A special thanks also to Prof.Yuri Ovchinnikov, since the research that is the subject of this thesis work is started with our collaboration when he spent some months in Naples.
And now I would thank all the people who were next to me during these three years: all the friends from the Emergency group, and expecially Germana, Giovanni e Gigi. I would thank all my friends and a special thanks is for Flavia, Paolo, Fabio, Sebastiano. I would thank also Luigi Longobardi for his friendship and for supporting me during this thesis work.
Et je voudrais même remercier mes amis françaises, et en particulier Magali, Julie et Abdel...ma permanence à Grenoble n'aurait pas été ainsi belle sans de vous!
I wish thank also two special friends: Silvia Bergamini and Elva Torres. Even if you live far away from me, you are always present in my life and ready to listen to me.
I would tank Guido Celentano for his assistance, that goes always beyond the bureaucratic task.
And finally I would like to give my special thanks to my parents and my brother, because they constantly encouraged me and let me smile. You'll be always a point of reference for me.

Introduction

This thesis focuses on macroscopic quantum phenomena in superconductivity, that, thanks to nanotechnology, are going to belong to everyday life.
Since quantum mechanics was shown to be successful in explaining some experimental anomalies for single electrons, photons and atoms at the beginning of last century, the limits of its validity have been investigated. Quantum mechanics is more than just a "theory": it is a completely new way of looking at the world.
As well known, Schrödinger proposed a theoretical experiment where a microscopic two-state system, for which quantum mechanics is supposed to be valid, is linked to a macroscopic system (a cat), which is supposed to behave classically. In this way the fate of the cat (alive or dead) is linked to the state of the quantum two state system ($|\ 0\rangle$ or $|\ 1\rangle$). The conclusion that a superposition of the quantum system would lead to a superposition of the cat's fate was the beginning of new and numerous discussions about the interpretation of quantum mechanics. The search for evidence of macroscopic quantum phenomena has been pursued in many different areas of physics, but the study of superconducting devices has been the one in which the programme has been more systematic and successful, since these devices, based on the Josephson effect, are promising candidates, as suggested in 1980 by Caldeira and Leggett. Their advantages include the fact that the classical dynamics of the relevant macroscopic variable is well note, that the "in-

trinsic" dissipation associated with the motion of this variable can be made extremely weak by going to low temperatures and finally that this variable can be addressed by electromagnetic means using technology already familiar to electrical engineers.

Moreover the concept of Nanotechnology began to be popular when Richard Feynman, more than 40 years ago, gave a famous talk entitled *Plenty of room at the bottom*, at the 1959 APS meeting. This talk induced a lot of scientists to study the machines at the nanometer scale.

The growing interest in nanoscience is partially due to its promise for new devices offering functionality attainable with small micro or nano-mechanical systems. In fact, at even higher frequency, even smaller size scale, it is possible to overcome the barrier between classical and quantum regimes. Ultimate realization of this will require parallel development of carefully engineered technology and deeper scientific understanding. So it is possible to say that the Feynman's visionary predictions are becoming reality. Moreover it is worth noting that this emerging field has some practical applications, and many more could be found.

This thesis focuses on answering the question of how quantum mechanical devices might be used to investigate the macroscopic quantum phenomena by using an external microwave irradiation, and in particular the photon assisted tunneling is studied here. In chapter 1 the process is analyzed from a theoretical point of view. Then the process has been investigated experimentally. In chapter 2 a study for microwave filtering at low temperature, where different devices have been investigated, in order to improve the filtering for the dilution cryostat setup. In chapter 3 experiments performed on micro-structured samples carefully isolated from external noise are reported. Finally, measurements on SQUID-based devices realized in the thermal and in the quantum regime are presented. The cooling has been realized by using respectively a ^{4}He cryogenic system and a ^{3}He/^{4}He dilution cryostat.

Chapter 1

Theory for microwave induced quantum phenomena in Josephson devices

In this chapter I present a new theoretical approach to describe the quantum behavior of a macroscopic underdamped system [1] interacting with an external field at frequencies close to resonant condition.

1.1 Low viscosity limit

The physical reason for viscosity is the interaction of an external degree of freedom with the thermal bath. The influence of viscosity on tunneling probability is of special interest since quantum tunneling of a particle interacting with a thermal bath is essential in many phenomena. For a theoretical and experimental investigation of this phenomenon it is convenient to use the Josephson effect, since the form of the potential is known for many different devices and their parameters can be found experimentally.
Resonance phenomena, that are expected to happen whenever two levels in

adjacent wells cross under the influence of an external bias, will be studied here. For bias values corresponding to a crossing of energy levels, it is possible to neglect processes in the reverse direction, provided that the temperature is sufficiently low.
Here I'll consider the resonant tunneling assisted by microwave irradiation in two different regimes: the moderate underdamped quantum regime [2] and in the extreme underdamped limit [3]. The analysis has been done by using density matrix formalism [4] and all calculations have been performed in the quasiclassical approximation (details are reported in [5, 6]).
As macroscopic quantum system here I consider an rf SQUID, that is a superconductive ring interrupted by one Josephson junction. This system presents a double-well potential [A.1]. The transition probability from the left well to the right one can be generally due to two different processes:

- *classical thermal activation* over the barrier top
- *quantum tunneling* through the barrier

The process is classical or quantistic depending on the temperature. For this study I considered the case T=50 mK, that is below the device crossover temperature, so that the quantum tunneling is the dominating process.
For an rf SQUID in these conditions the existence of Quantum Levels has been experimentally confirmed [7, 8, 9, 10]. Existence of levels becomes evident because of reduction of the lifetime of a metastable state under the action of an external current corresponding to a frequency equal to the distance between energy levels.
In the considered case, energy states can be visualized as belonging to different wells of the potential and the transition process is dominated by quantum tunneling across the potential barrier. The non-zero width of levels leads to a loss of coherence during the tunneling process [11, 12] and in such a case the behavior of the system strictly depends on the ratio between the two

small parameters γ and T_P, where γ is connected to the width of quantum levels $\hbar\gamma$ and T_P is the tunneling amplitude.
Control of the quantum device state can be achieved by using microwave irradiation to induce transitions from the ground state to higher energy states [13].
It is possible to define three different regimes for the tunneling process:

- *overdamped regime*, with $\hbar\gamma \gg \hbar\omega_0$
- *moderate underdamped regime*, with $\hbar\gamma \ll \hbar\omega_0$ and $\gamma \gg T_P$
- *extremely underdamped regime*, with $\hbar\gamma \ll \hbar\omega_0$ and $\gamma \ll T_P$

where ω_0 is the plasma frequency for the rf SQUID (defined in eq.(3.10)) and $\hbar\omega_0$ is the energy difference between the two levels.
In order to study quantum resonant phenomena it is necessary to minimize the interaction between the device and the environment, since this interaction leads to a finite width $\hbar\gamma$ of quantum levels [14, 15] and resonant phenomena can occur only if the energy width is small compared to the energy difference between levels ($\hbar\gamma \ll \hbar\omega_0$).
The theory has been developed considering the case resonant phenomena are induced by using an external pumping with frequency $\nu = \omega/2\pi$ and amplitude $\mathcal{I}$.
The hamiltonian describing the rf SQUID in the presence of an external field with pulsation ω and amplitude $\mathcal{I}$ is

$$H_0 = -\frac{1}{2M}\frac{\partial^2}{\partial\varphi^2} + U_0\left[\frac{1}{2M}\left(\varphi - \varphi_x\right)^2 + \beta_L\cos\varphi\right] + \frac{\mathcal{I}}{2e}\cos(\omega t)\varphi \qquad (1.1)$$

where as usual φ_x is the external magnetic flux, M is the "mass" of the junction

$$M = \left(\frac{\hbar}{2e}\right)^2 C \qquad (1.2)$$

and C is the junction capacitance. In eq.(1.1) quantities U_0 and β_L are experimental parameters of the system and are defined as

$$U_0 = \left[\left(\frac{\Phi_0}{2\pi}\right)^2 \frac{1}{L}\right] \tag{1.3}$$

$$\beta_L = \frac{2\pi L I_c}{\Phi_0} \tag{1.4}$$

The first two terms of eq.(1.1) correspond to the normal hamiltonian for a rf squid, while the third part describes the external microwave, as it is evident by comparing eq.(1.1) and eq.(A.7).
Following a common practice [16], the dimensionless variable φ_x is obtained by referring the magnetic flux to $\Phi_0/2$ and normalizing it to $\Phi_0/2\pi$. Here the external flux φ_x is used as a free parameter, that in numerical calculations is varied around a critical point $\varphi_x^{(0)}$ in order to control the dynamics of the system, while U_0 and β_L are fixed.
The dissipation is accounted for by an effective resistance R_{eff} [A.3] in the RSJ model for the junction [17]. So a bigger R_{eff} implies a better insulation [17], that means a smaller width of the levels.

1.2 The moderate underdamped regime

The *moderate underdamped quantum regime* corresponds to the case when the conditions $\gamma \gg T_P$ and $\gamma \ll \omega_0$ are both satisfied. This process can be visualized as a two-steps process starting from the ground state in the left well: there is first a resonant pumping from the ground state to an excited level and then a resonant tunneling from left to right well.
The condition $\gamma \gg T_P$ assures that the excited level in resonance with the microwave is not too close to the top of the potential barrier so that thermally induced decay between levels in the same well is the dominant transition with respect to the tunneling process. In fact the macroscopic tunneling can be

observed only if the number of levels in the left potential well is not too large [5].

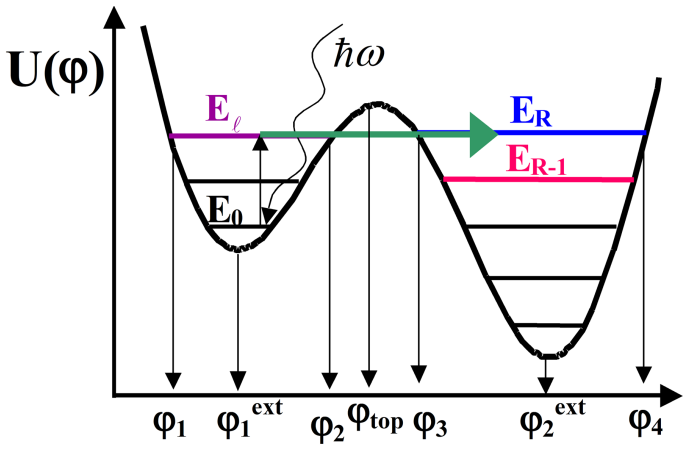

Figure 1.1: A sketch of the double-well potential U(φ) for an rf SQUID in the moderate underdamped limit. Here horizontal lines are quantum levels. The two minima are located at φ_1^{ext} and φ_2^{ext}, while φ_{top} is the position of the potential maximum. The turning points for the energy levels E_ℓ, and E_R are φ_1, φ_2 and φ_3, φ_4, respectively.

For numerical calculations I used the following parameters:

- $\beta_L = 1.75$
- C = 0.1 pF
- L = 210 pH
- $R_{eff} = 8$ MΩ
- T = 50 mK.

and pumping frequencies ranging from $\nu = \omega/2\pi = 25.1$ GHz to $\nu = 25.8$ GHz.

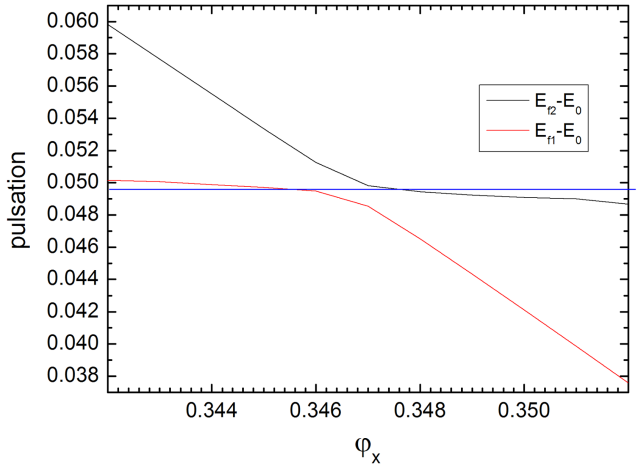

Figure 1.2: Picture of energy curves E_{f_1}-E_0 and E_{f_2}-E_0 in this regime and for the parameters considered above. In this display ω values are horizontal lines.

These parameters were chosen in order to assure that the excited pumped level in the left potential well is close to a level in right potential well and that they are in resonant conditions.
The frequency range has been determined by looking at the energy curves E_{f_1}-E_0 and E_{f_2}-E_0. It is possible to observe two peaks only for ω values that intersect both the energy curves (Fig.1.2).
The transition probability W from the left potential well to the right potential well has been numerically calculated for a rf SQUID as function of the external flux φ_x. In this regime and in this frequency range the transition probability W, as shown in Fig.1.3, presents two peaks: the position of peaks is connected with the resonance tunneling and does not depend on the resonance pumping, whereas the second one is associated with the resonance pumping and its position varies by varying the frequency (details are

reported in [1, 2]).

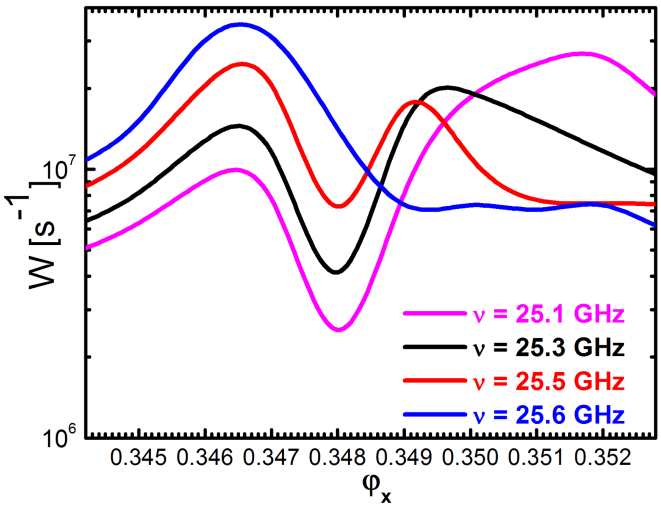

Figure 1.3: Transition probability W as function of φ_x for different values of the pumping frequency. The two peaks are connected to effects of the resonant tunneling between levels in different wells and the resonant pumping between levels in the same well. The peak due to the resonant pumping moves with the pumping frequency until it superimposes to the tunneling peak. Curves are obtained by using following parameters: β_L=1.75, L=210 pH, C=0.1 pF, and R=6 kΩ.

1.3 The extremely underdamped regime

The second case presented here is the small viscosity limit, that corresponds to the case when conditions $\gamma \ll T_P$ and $\gamma \ll \omega_0$ are both satisfied, and it is referred as the *extremely underdamped regime*. In these conditions, if we consider two levels, in different wells, that are in resonance, a coherent superposition of distinct states can occur and a gap Δ appears between these energy levels. As a consequence the wave functions, related to these energy

levels, spread all over the two wells, generating delocalized states with energies E_{f_1} and E_{f_2}.
For each device there's a frequency range for the external microwave such that, in the extremely underdamped limit it is possible to observe three peaks in the transition probability distribution. The frequency range has been determined by looking at the energy curves E_{f_1}-E_0 and E_{f_2}-E_0.

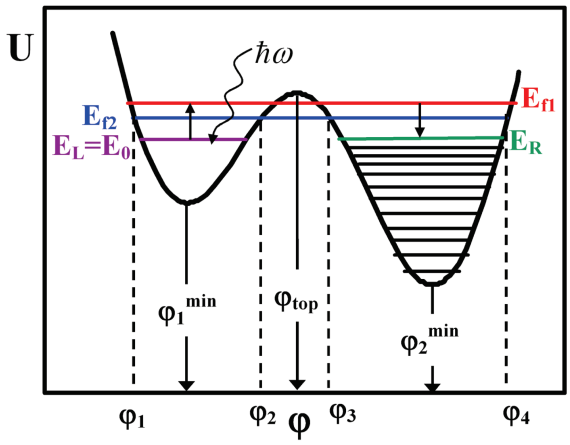

Figure 1.4: A sketch of the double-well potential U(φ) for the considered device, an rf SQUID, in the extremely underdamped limit. Here horizontal lines are quantum levels. Here are plotted the ground level in the left well with energy E_0, the resonant level in the right well with energy E_R, and the two delocalized states characterized by energies E_{f_1} and E_{f_2}.

In fact it is possible to observe two peaks only for ω values (represented as horizontal line in Fig.1.5) that intersect both the energy curves. For a fixed value of the pumping ω in this range, the central maximum is due to the resonance tunneling and the two others are due to the resonant pumping of the two levels close to the barrier top (see Fig.1.6).

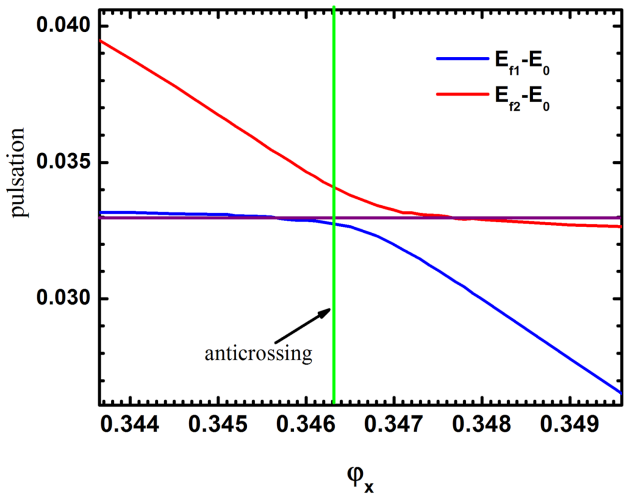

Figure 1.5: Curves E_{f_1}-E_0 vs. φ_x and E_{f_2}-E_0 vs. φ_x. All energies are referred to the barrier top. The horizontal line is the external field with pulsation ω, it crosses the energy curves E_{f_1}-E_0 and E_{f_2}-E_0 in two points. The vertical line represents the coordinate corresponding to the anticrossing point. Comparison of Figs.1.5-1.6 shows that the first peak correspond to the resonant pumping from the ground state in the left well to the state with energy E_{f_1} while the third peak corresponds to the resonant pumping from the ground state to the state with energy E_{f_2}. Curves are obtained by using following parameters: β_L=1.75, C=0.1 pF, L=210 pH.

The central peak is fixed in position, whereas the two lateral peaks move by varying the frequency.
If we consider an ω value that is outside from this range, transition probability curve has only one peak, as usual, as shown in Fig.1.7.

Some numerical calculations have been made in order to understand the dependence of the transition probability W on the different parameters in this regime. First I studied the dependence of the peaks on the effective dissipa-

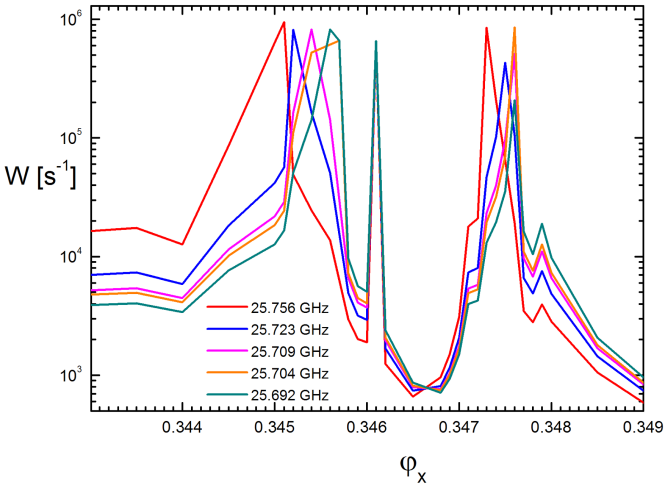

Figure 1.6: Transition probability W vs. φ_x for different values of the pumping frequency ν. The central maximum is due to the resonance tunneling and two lateral peaks are related to the resonant pumping. Curves are obtained by using the following parameters: β_L=1.75, L=210 pH, C=0.1 pF, and R_{eff}=8 MΩ.

tion described in the RSJ model [17] by the effective resistance R_{eff} [A.3]. As expected [18], by decreasing dissipation, that is by increasing R_{eff}, peaks resolution is enhanced (Fig.1.8).

I also performed some numerical calculations to study the transition probability W vs. φ_x for different β_L values. It is worth noting that to vary the β_L value, I varied only the value of the inductance L (see eq.1.3) and a variation of β_L corresponds to the variation of the height of the potential barrier. I found that, when the β_L value increases, the transition probability becomes smaller and the external parameter φ_x has to be increased in order to observe the peaks. Details for calculations are reported in [19].

It is worth noting that only levels below the top of the classical energy bar-

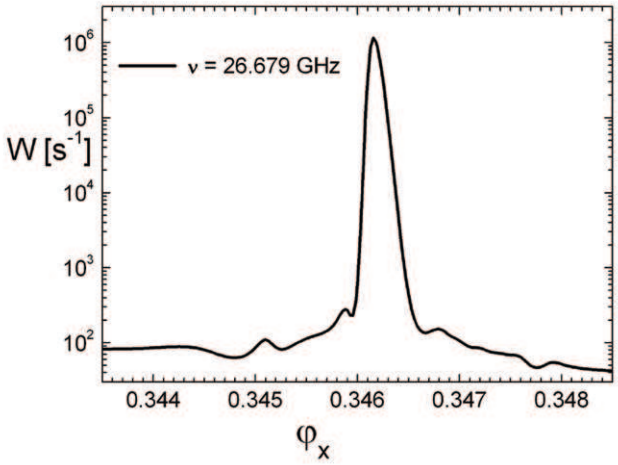

Figure 1.7: Transition probability W vs. φ_x. Here the W presents only one peak due to the resonance tunneling. The plot has been obtained by using the following parameters for the numerical simulation: β_L=1.75, L=210 pH, C=0.1 pF, and R_{eff}=8 MΩ.

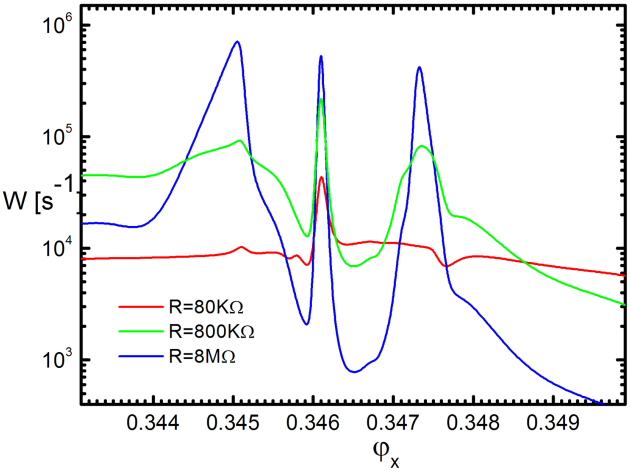

Figure 1.8: Transition probability W vs. φ_x for different values of the effective resistance R_{eff}. The plot has been obtained by using the following parameters for the numerical simulation: β_L=1.75, L=210 pH, C=0.1 pF, ν= 25.756 GHz.

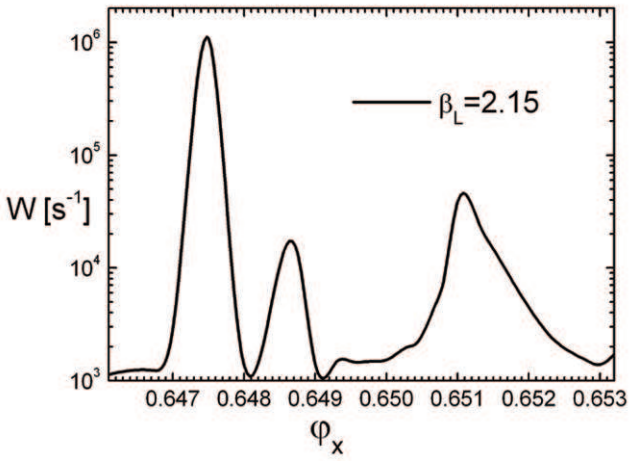

Figure 1.9: Transition probability W vs. φ_x for β_L=2.15, L=258 pH, C=0.1 pF, R_{eff}=8 MΩ and ν= 32.818 GHz.

rier have been considered here. This condition is essential, since in this case energy levels (in the absence of coherence) can be exclusively associated with one well and moreover it is a necessary condition in order to observe tunneling phenomena.

Obtained results suggest that resonant quantum tunneling is a convenient tool to investigate macroscopic quantum phenomena.

Predicted phenomena can be observed by escape rate measurements [8], as described in chapter 3. It is worth noting that in considered problems friction has a relevant role in both regimes since it leads to a finite width γ of levels and destroys the coherence by tunneling [20]. In both regimes peaks position strictly depends on the pumping frequency and on the external flux biasing the rf SQUID.

As a future improvement it could be interesting to study the cases with a different number of levels in left well. In such a case the theory that describes the system should be slightly modified.

Chapter 2

Microwave filtering stage for Josephson devices

In order to realize measurements with SQUID-based devices I have realized a study in Grenoble, at the Centre de Recherches sur les Très Basses Températures (CRTBT) - CNRS. Final goal of this study is to understand and optimize the behavior of a resonant circuit in order to study quantum phenomena in presence of a microwave excitation with a greater evidence.
A preliminary request to study quantum phenomena and perform quantum measurements at cryogenic temperatures, is to use a low microwave power. Then it has been necessary to have a special care about noise [21, 22] in order to filter all the possible noise generated by electronic devices that work at cryogenic temperature. Finally it has been necessary to avoid spurious reflections of the microwave signal. So, before sending the signal to the device of interest, it is compulsory to use some intermediate stage. I have chosen a circulator and an insulator, that are non-symmetric devices: this means that a signal can pass through them without attenuation in one direction, while it is strongly attenuated in the other one.
Since a low microwave power has been used, it has been necessary to intro-

duce an amplifier as a final stage, before the readout.
As future improvement we would use a microwave generator to obtain some pulses for a time interval Δt, instead of a Vector Network Analyzer.
In this chapter the scheme used for measurements and the related cryogenic apparatus, that have been especially developed for this experiment, will be described. The final goal of this study is the realization of a resonator coupled to the device [23, 24], in order to optimize the signal to noise ratio (S/N). In Fig.2.1 there is the scheme realized for this study.

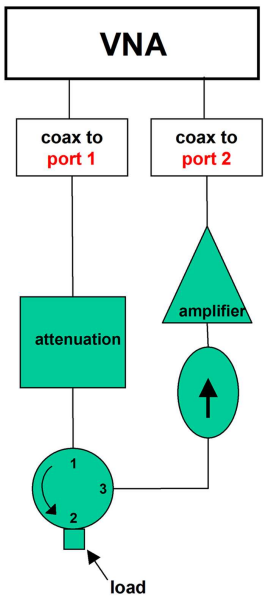

Figure 2.1: Picture of the final scheme for the filtering stage.

2.1 Theoretical calculations

Some calculations have been performed in order to understand how to realize the conditions to have the energy equivalent to a single photon inside the

resonator, in the final configuration.
The quality factor for a resonant circuit, that in this case is equivalent to a RLC parallel circuit, is defined as the *resonant pulsation* ($\omega_p = 2\pi\nu_p$) multiplied for the *energy stored* by the resonator (U_S) and divided by the *average power loss* (P_L) in the resonant circuit:

$$Q = \omega_p \frac{U_S}{P_L} \tag{2.1}$$

Here the ideal case has been considered, that is when average power loss in the resonant circuit is all the power that arrives on the device, that is the power generated by the VNA minus the attenuation.
First I calculated the quality factor for the LC resonator having a characteristic resonant frequency ν_p=10.24 GHz. I considered the littlest power I can use, that is to say P = -65dBm, with attenuation equal to -40dB, that is P^{IN}=-105 dBm = $3.16 \cdot 10^{-14}$W. Using ω_p=2π10.24 GHz, the stored energy for one photon is $\hbar\omega_p$. By using these values the Q factor is equal to Q = 13.82, that is quite low.
So I calculated the power that is necessary with this device in order to obtain a Q factor equal to 10^4 and I found P^{IN}=-135dBm, that means to use an higher attenuation, equal to -70dB. In this case the ratio S/N becomes much more noteworthy.

2.2 Measurement Setup

2.2.1 The Vector Network Analyzer

Vector Network Analyzers (VNA) is an instrument used to measure components, devices, circuits. It contains both a source and multiple receivers, and moreover it can display amplitude and phase information. Finally with vector-error correction the VNA provides a better measurement accuracy

than spectrum analyzers, as i will describe in the following.
VNA can measure the complex transmission and reflection characteristics of two-port devices in the frequency domain. It does this by sampling the incident signal, separating the transmitted and reflected waves, and then performing ratios that are directly related to the reflection and transmission coefficients of the two-port. Frequency is swept in order to rapidly obtain amplitude and phase information over a band of frequencies of interest.
VNA hardware consists of a sweeping internal signal source, a test set to separate forward and reverse test signals, and a multi-channel, phase-coherent, highly sensitive receiver.
Here the microwave power is expressed in dBm, that is an abbreviation for the power ratio in decibel (dB) of the measured power referred to one milliwatt (mW), so if we consider power P=0.001W it is equivalent to 0 dBm. Moreover, since it is referred to the watt, it is an absolute unit and it is convenient because of its capability to express both very large and very small values in a short form. For these measurements I used the Vector Network Analyzer HP 8720B.
For all the measurements presented here a low power for the microwave signal has been used, in order to do a preliminary study to perform quantum measurements.
Electrical devices that can be characterized using VNA include both passive and active devices. Examples of passive devices are resistors, capacitors and inductors, splitters, directional couplers and attenuators. Active devices would include transistors, oscillators, radio-frequency integrated circuits and modulators. I made both the kinds of measurements, since I started by measuring some simple components and then I studied a more complex scheme, including all these devices and a resonator.
Even if for some of these devices magnitude-only measurements are sufficient, I measured, for them at all, the real and the imaginary part of the signal, in

order to study the reflection coefficient Γ defined as the ratio of the reflected signal voltage to the incident signal voltage, as following:

$$\Gamma = \frac{V_{reflected}}{V_{incident}} = \rho e^{i\phi} = \frac{Z_L - Z_0}{Z_L + Z_0} \tag{2.2}$$

where Z_L is the load impendence and Z_0 is the VNA impendence, that is 50Ω. All these measurements were performed by using the Smith Chart.

The S-parameters

The scattering matrix is a mathematical construct that quantifies how RF energy propagates through a multi-port network. The S-matrix allows to accurately describe the properties of networks as simple "black boxes". For an RF signal incident on one port, some fraction of the signal bounces back out of that port, some of it scatters and exits other ports (and is perhaps even amplified), and some of it disappears as heat or even electromagnetic radiation.

S-parameters are complex (magnitude and angle) because both the magnitude and phase of the input signal are changed by the network. S-parameters vary as a function of frequency for any non-ideal network.

For the S-parameter subscripts "ij", j is the port that is excited (the input port), and "i" is the output port. Parameters along the diagonal of the S-matrix are referred to as reflection coefficients because they only refer to what happens at a single port. Thus S_{ii} refers to the ratio of signal that reflects from port "i" for a signal incident on port "i". Off-diagonal S-parameters are referred to as transmission coefficients, because they refer to what happens from one port to another.

S-parameters describe the response of an N-port network to voltage signals at each port.

If we consider a two-port device and we define the incident voltage at each

port is denoted by "a", while the voltage leaving a port is denoted by "b", it is possible to find the following relationship:

$$\begin{aligned} b_1 &= S_{11}a_1 + S_{12}a_2 \\ b_2 &= S_{21}a_1 + S_{22}a_2 \end{aligned} \tag{2.3}$$

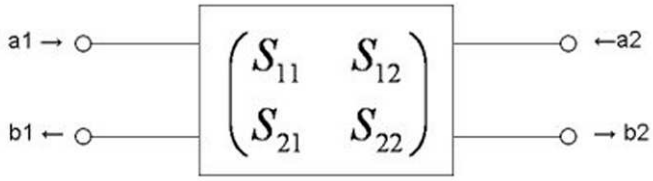

Figure 2.2: A simple scheme to display the S-parameters for a two-port device.

In this case the S matrix is a matrix [2x2], which elements are defined as:

$$S_{ij} = \frac{b_i}{a_j}|_{a_k=0, k\neq j} \tag{2.4}$$

By using the eqs.2.3 it is possible to define the four S-parameters of the 2-port device as:

$$S_{11} = \frac{b_1}{a_1}$$
$$S_{12} = \frac{b_1}{a_2}$$
$$S_{21} = \frac{b_2}{a_1}$$
$$S_{22} = \frac{b_2}{a_2}$$

Finally it is useful to remind that S-parameter magnitudes can be presented in two ways: linear magnitude or decibels (dB). S-parameters are a voltage ratio, so the formula for decibels in this case is

$$S_{ij}(dB) = 20 * log[S_{ij}(magnitude)]$$

It's worth noting that the whole measuring process accuracy depends on the accuracy of the S-parameters measurements and this depends on the calibration. Moreover the calibration process allows to recognize systematic errors (that are repeatedly and therefore predictable) and then mathematically remove them during the measurements. Anyway it is impossible to remove the random errors, due for example to the noise. Finally it is also important to consider the drift errors due, for example, to the temperature variation, but these can be removed by performing a new calibration.
I used to do a new calibration just before of each set of measurements, since the measurements could vary even moving the cable.

The *dynamic range*

The *dynamic range* is usually defined as the maximum power the receiver can accurately measure minus the receiver noise floor. Usually at least 80 dB dynamic range is requested to proper characterize the rejection characteristic of the filter. The dynamic range is really important for measurement accuracy. The dynamic range for transmissions measurements for the HP8720B is equal to 80 dB between 0.5 GHz and 2 GHz, and it is equal to 85 dB between 2 GHz and 20 GHz.
Measurements have been performed by using a narrow IF filter (300 Hz, 100 Hz or 10 Hz) in order to produce a lower noise floor and assures a significant sensitivity improvement. Moreover I also utilized the averaging function, with 16 averages. This method allows also to to eliminate harmonic and spurious response. In fact the RF signal is downconverted and filtered before it is measured and so the harmonics associated with the source are also downconverted, but they appear at frequencies outside the IF bandwidth and are therefore removed by filtering.
An alternative method could be to increase the power, but this is not useful in order to realize a study in the quantum regime.

Vector-error correction

Vector-error correction is the process of characterizing systematic error terms by measuring known calibration standards and then removing the effects of these errors from subsequent measurements.
One-port calibration is used for reflection measurements while the full two-port calibration can be used for both: reflection and transmission measurements.

2.3 Measurements on single components

2.3.1 Parameters

It's possible to realize many different configurations, so that is useful to define some parameters in order to compare them.
In Fig.2.1 it is reported the final scheme we want to measure. It's possible to define three ports:

- port 1: the input port, that is port 1 for the VNA.
- port 2: the load port, here we'll place the device we want to study.
- port 3: the readout port, that is port 2 for the VNA.

With three ports it is possible to define nine parameters, as in the following:

- $\mathcal{S}_{11}$ is the reflection on the input port. It should be minimized.
- $\mathcal{S}_{21}$ is the transmission from the input port to the device. It should be maximum.
- $\mathcal{S}_{32}$ is the transmission from the device to the readout port. It should be maximum.

- $\mathcal{S}_{12}$ is the transmission from the device to the input port. It should be minimized.

- $\mathcal{S}_{23}$ is the transmission from the readout port to the device. It should be minimized.

- $\mathcal{S}_{33}$ is the reflection on the readout port. It should be minimized.

The object of the study is the total transmission parameter $\mathcal{S}_{31}$ defined as the sum of the two partial transmission

$$\mathcal{S}_{31} = \mathcal{S}_{32} + \mathcal{S}_{21} \tag{2.5}$$

Moreover it is necessary to choose a threshold to evaluate the behavior. As will be evident in the following, it is necessary to use different criteria at different temperatures. So at room temperature (T=300K) the criteria I chose is to have 25 dB difference between transmitted and reflected signal.
At nitrogen temperature (T=77K) it has been necessary to establish a threshold less significative, of the order of 15 dB. Finally at helium temperature (T=4.2K) the threshold I could state has been 10 dB.
By using these criteria I measured the different components that are necessary to realize the final scheme. I compared different configurations and I chose the best ones with respect to the established criteria.
In the following graphics the reflection coefficients $\mathcal{S}_{11}$ and $\mathcal{S}_{33}$ are always respectively in red and in magenta. The transmission $\mathcal{S}_{31}$ is always in blue, while the transmission in the opposite direction $\mathcal{S}_{13}$ is displayed in green.

2.3.2 The circulator

Circulators are realized by using properties of non reciprocal junction. They are passive devices with three or more ports in which the ports can be accessed in such an order that when a signal is fed into any port it is transferred

to the next port, the first port being counted as following the last in order. In a circulator each port is coupled with the following one and completely decoupled by the others. Usually a non reciprocal junction is realized by using the electromagnetical properties of ferrite. This material in fact is really sensitive to the direction and to the frequency of the electromagnetical field.
For this study two different circulators have been measured, one from the MCLI and the second one by the AEROTEK. Both the circulators I studied present three ports. Their characteristics are reported respectively in Table 2.1 for MCLI insulator and in Table 2.2 for AEROTEK insulator.

MCLI circulator		
T	25C	-54C to +85C
Frequency Range	8.0-12.0 GHz	8.0-12.0 GHz
Isolation (Min)	23 dB	20 dB
Insertion Loss (Max)	0.45 dB	0.50 dB
VSWR (Max)	1.18	1.25
Peak Power	250 W	250 W
Average Power	25 W	25 W

Table 2.1: Technical characteristics for the MCLI circulator

Experimental tests

I studied different configurations in order to find the best one with respect to the parameters established before. I used the “full 2 ports” calibration including the coax and the two sharp bends and one connection female-female, that is necessary in order to do the transmission test in the calibration process. The calibration was done using following parameters:

AEROTEK circulator		
T	25C	-54C to +85C
Frequency Range	8.0-12.0 GHz	8.0-12.0 GHz
Isolation (Min)	23 dB	20 dB
Insertion Loss (Max)	0.45 dB	0.50 dB
VSWR (Max)	1.18	1.25

Table 2.2: Technical characteristics for the AEROTEK circulator

Power	-10 dBm
IF filter	300 Hz
AVG	no average
no. of points	1601

Table 2.3: Parameters used for the calibration and for the measurements of the two circulators, in all the configurations.

The MICLI and AEROTEK circulator have been measured by using the same schemes and I found that the AEROTEK circulator works better at low temperature. For this circulator *configuration C*, showed in the Fig.2.3, is the best one in order to realize the final setup. This configuration has been introduced in order to perform low temperature measurements including the insulator and the cryogenic amplifier, as explained in the next sections.
As described in the scheme, I used a short on port 2, so that all the signal is reflected and the losses are almost zero. In this configuration the two matrix elements that describe the transmission, $\mathcal{S}_{13}$ and $\mathcal{S}_{31}$, are almost the same, even if it is possible to observe that $\mathcal{S}_{13}$ is a little bit greater than $\mathcal{S}_{31}$. This is due to the behavior of the circulator. In fact in $\mathcal{S}_{31}$ the signal arrives from port 1, then it goes on port 2 and it is completely reflected because of the short. Finally it goes on the port 3 and it is read by VNA. On the other side

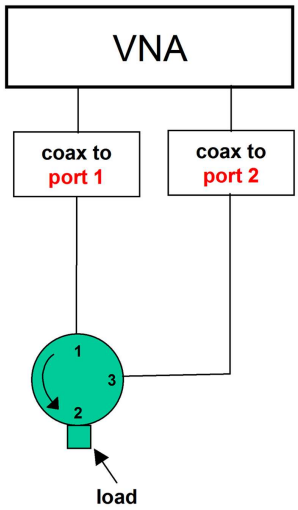

Figure 2.3: Scheme to measure the circulator in configuration C

in $\mathcal{S}_{13}$, the signal arrives from port 3, than it goes on port 1 and is read from the VNA, while the port 2 is completely ignored, so that the attenuation is lower.

First I performed the measurements at room temperature (300 K) for all the four parameters of the scattering matrix, as reported in the Fig.2.4. Then I repeated the measurements at nitrogen temperature (77 K), the result is reported in the Fig.2.5. In order to perform the measurements in helium (T=4.2 K) it was necessary to perform a different calibration that includes only the blue cables. In Fig.2.6 it is displayed the comparison between measurements at room and helium temperature with this new calibration.

It's evident that in both cases the behavior of the device is worst at lower temperature. In fact, as for the circulator, the bandwidth becomes smaller, and it is necessary to choose a lower threshold. This effect becomes much more evident at lower temperature. In measurements at T=4.2 K there is a further attenuation equal to -10 dB, due to coax cables, as I verified. In

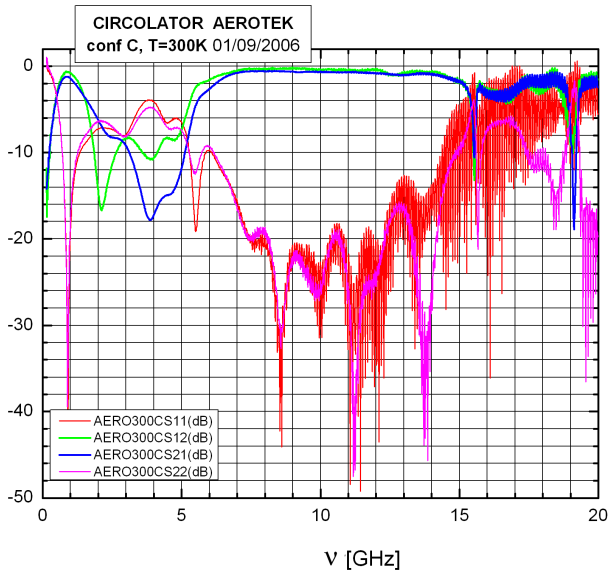

Figure 2.4: Measurements at T=300K for configuration C as a function of frequency ν. The transmission coefficients $\mathcal{S}_{31}$ (blue) and $\mathcal{S}_{13}$ (green) are about 25 dB greater than reflection coefficients $\mathcal{S}_{11}$ (red) and $\mathcal{S}_{33}$ (magenta).

Fig.2.7 are displayed the curves for the transmitted signal for the coax cables at T=300K (red line) and at T=4.2K (blue line).

From Fig.2.7 it is evident that there's a strong attenuation for increasing frequency and that the attenuation at ν =10 GHz is about 10dB at T=4.2K.

The AEROTEK insulator

Then I studied the behavior of an *insulator*. An insulator is a non reciprocal junction that presents an attenuation value on one direction and a different one in the opposite direction. In fact the attenuation is almost zero in one direction, while is really high in the other one. Usually insulators are realized, like circulators, by using the electromagnetical properties of ferrite.
Here I report the specifications for the AEROTEK insulator:
An insulator can be realized by using a circulator where the third port has

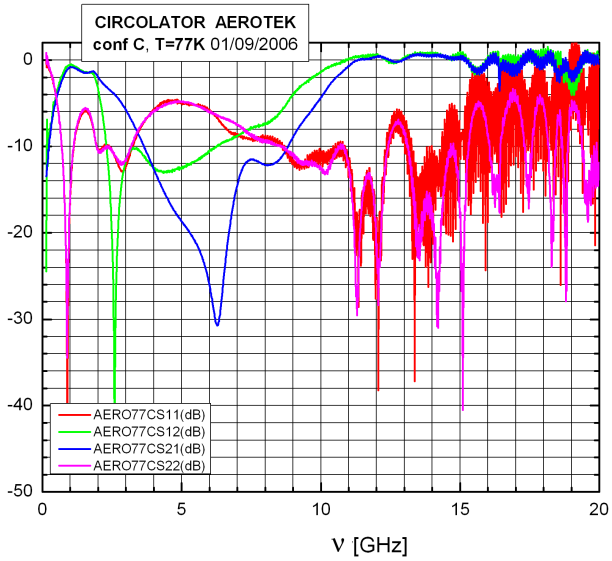

Figure 2.5: Measurements at T=77K for configuration C as a function of frequency ν. Here transmission coefficients $\mathcal{S}_{31}$ (blue) and $\mathcal{S}_{13}$ (green) are about 15 dB greater than reflection coefficients $\mathcal{S}_{11}$ (red) and $\mathcal{S}_{33}$ (magenta).

AEROTEK insulator	
Frequency Range	9.5-10.5 GHz
Isolation (Min)	23 dB
Insertion Loss (Max)	0.4 dB
VSWR (Max)	1.15

Table 2.4: Technical characteristics for the AEROTEK insulator

been closed on a resistance equal to 50Ω.

Experimental test

For the insulator only one configuration was possible and is shown in Fig.2.8. The transmission has been studied by using the parameter $\mathcal{S}_{31}$, since it works better than $\mathcal{S}_{13}$. The results for measurements at T=300K are reported

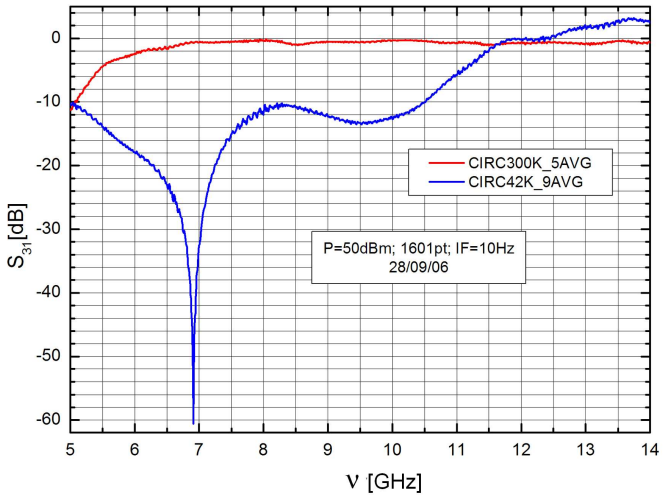

Figure 2.6: Measurements at room and helium temperature for the AEROTEK circulator as a function of frequency ν. It is evident that it does not work between 7 GHz and 11 GHz, since in this region there's an evident attenuation.

in Fig.2.9 while the results for measurements at T=77 K are reported in Fig.2.10. Finally I measured the insulator at T=4.2 K, by using a different calibration (P=-65dBm; IF=10Hz, 1601 points). Results are showed in Fig.2.11. Here the curve at T=4.2 K presents a strong attenuation, due to the different calibration, that does not include the coax cables, whose behavior is illustrated in Fig.2.7.
As for the circulator, the behavior of the insulator becomes worse at lower temperature and the bandwidth becomes smaller, and it is necessary to establish a lower threshold.

Measurements including the circulator and the insulator

The scheme including the circulator so that the insulator is shown in Fig.2.12. I measured the four S-parameters at T=300 K and at T=77K
As attended, the total device, made up from the circulator and the insulator,

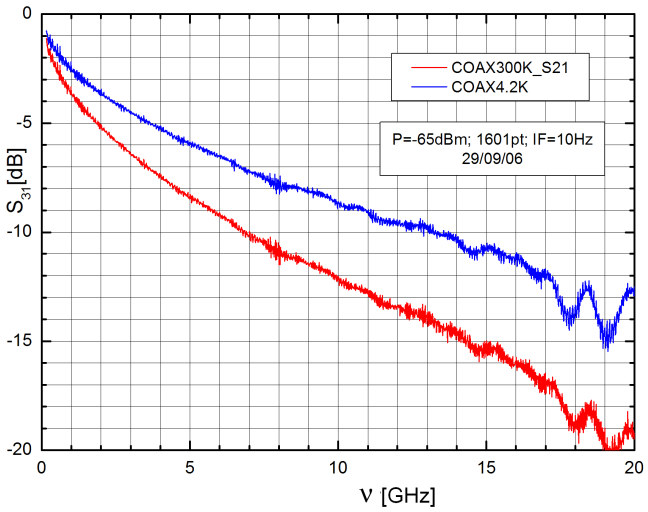

Figure 2.7: the transmitted signal for the coax cables at T=300K (red line) and at T=4.2K (blue line) as a function of frequency ν. There's a strong attenuation for increasing frequency.

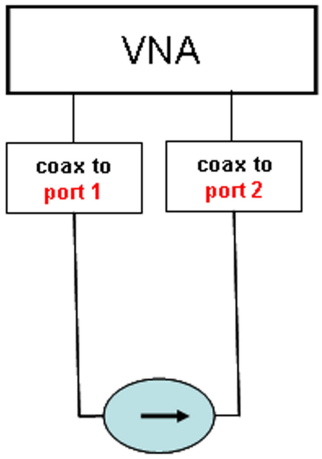

Figure 2.8: Schematics for the insulator

is described by a scattering matrix that is the product of the matrix of the single elements. This implies that if we consider the attenuation expressed

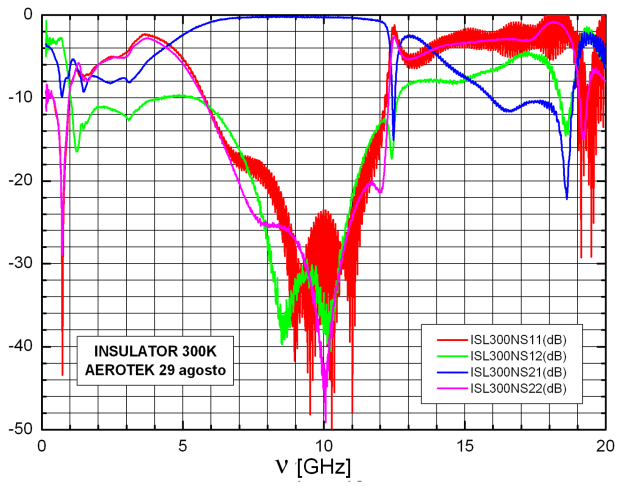

Figure 2.9: Measurements at T=300K for the insulator as a function of frequency ν. The transmission coefficient $\mathcal{S}_{31}$ (blue) is up to 25 dB greater than reflection coefficients $\mathcal{S}_{11}$ (red), $\mathcal{S}_{33}$ (magenta), and transmission coefficient in opposite direction $\mathcal{S}_{13}$ (green).

in dB, the total attenuation for *configuration C* is given by the sum of the attenuation due to the single devices, for each frequency value. This can be easily checked by comparing the transmission values in Fig.2.4, Fig.2.9 and Fig.2.13.

Comments

This study shows that the behavior of these devices is worse at lower temperature. This is due to the fact that these devices are not designed to work at low temperatures. By comparing different measurements for the two circulators it is evident that the MCLI circulator works better at room temperature, while at 77K the AEROTEK circulator is the best one.
By comparing the four parameters at different temperatures for each device, it is possible to observe a shift in the useful frequency window and this is

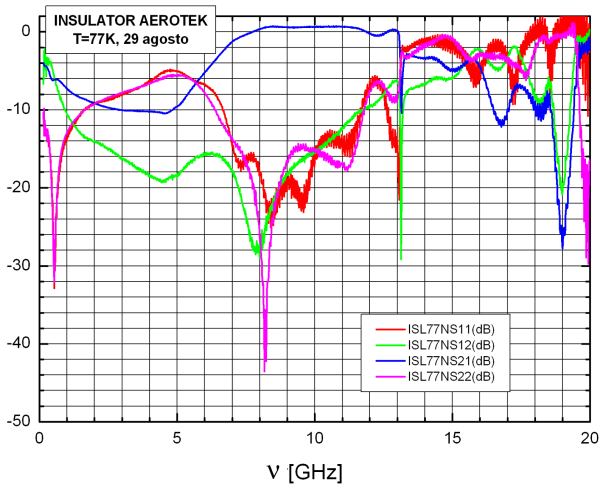

Figure 2.10: Measurements at T=77K for the insulator as a function of frequency ν. The transmission coefficient $\mathcal{S}_{31}$ (blue) is only 15 dB greater than other coefficients $\mathcal{S}_{11}$ (red), $\mathcal{S}_{33}$ (magenta), and $\mathcal{S}_{13}$ (green). It's evident that there is also a shift for all the curves.

probably due to the internal components.
It is worth noting that the shift has the same direction for the two circulators, even if they are of different brands, while it has different directions for the insulator and the circulator of the same brand, the AEROTEK. It could be interesting to compare this behavior with another insulator, in order to understand if this is a random or systematic behavior.
The thermalization time at T=77K and T=4.2K, is quite long, about 30 minutes, since these devices are not designed to work at low temperatures.
As it is evident by reading these devices characteristics, they introduce an attenuation along the electrical line. So, as a consequence of the low power used and of the further attenuation introduced by the circulator and by the attenuator, it is necessary to use an amplifier.

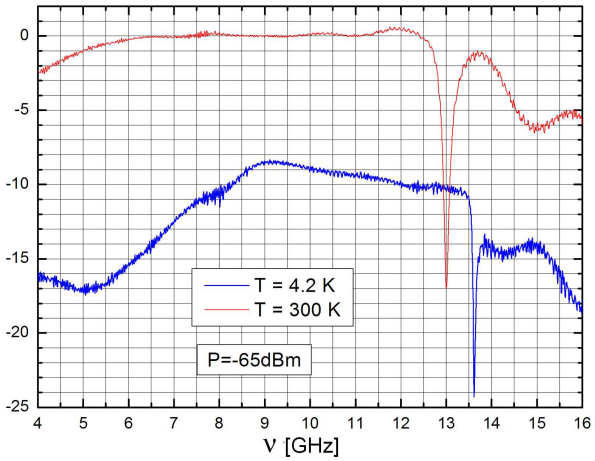

Figure 2.11: Measurements at T=4.2K for the insulator as a function of frequency ν. It's evident that there is a shift, while the attenuation is due to a different calibration, that does not include the coax cables.

2.3.3 The differential amplifier

For these measurements I used a standard low-noise amplifier by MITEQ, that is especially designed to operate in cryogenic environments. In fact MITEQ has supplied units cooled to liquid nitrogen temperatures (77 K), as well as units operating at helium temperature (4.2 K). These units utilize extremely low-noise amplifier designs, which are packaged in hermetically sealed kovar housings. Moreover these amplifiers are designed so that they can operate at much lower voltages, thus significantly reducing the total power dissipated by the devices within the amplifier. In Table 2.5 specifications for AFS4-08001200-10-CR-4 amplifier are reported:

However I measured the real current used and I found that at ΔV=6V the adsorbed current is I=88mA. This means that the dissipated power is P_W=0.528W.

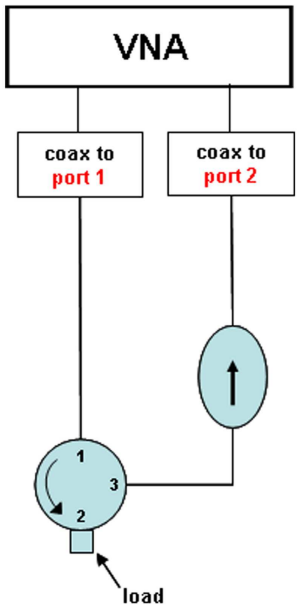

Figure 2.12: The scheme including the circulator and the insulator

AFS4-08001200-10-CR-4 cryogenic amplifier		
T	300K	77K
Frequency Range	8 12 GHz	8 12 GHz
Gain (dB, Min)	32	34
Gain Flatness (±, Max)	1 dB	0.75dB
Noise Figure (Max)	0.9 dB	0.35 dB
VSWR IN/OUT (Max.)	2:1	1.5:1
Output Power (Min.)	5 dB	5 dB
NOM. DC POWER (+6 V)	100 mA	100 mA
OUTLINE DRAWING	4	4

Table 2.5: Characteristics for the cryogenic amplifier.

In Fig.2.15 the scheme used to measure the amplifier at T=300K is reported. An attenuator equal to -20 dB has been introduced in the scheme in order

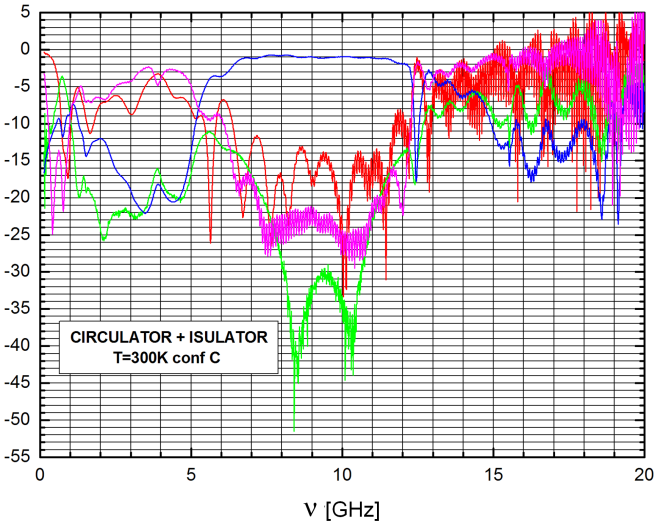

Figure 2.13: Measurements for the scheme including the circulator and the insulator at T=300K as a function of frequency ν. Here the transmission coefficient $\mathcal{S}_{31}$ (blue) is about 25 dB greater than other coefficients $\mathcal{S}_{11}$ (red), $\mathcal{S}_{33}$ (magenta) and $\mathcal{S}_{13}$ (green).

to consent to the VNA to read the output signal.
The amplifier response in the range 6 - 16 GHz, reported in Fig.2.16, has been obtained by using the scheme illustrated in Fig.2.15.

2.3.4 The cryogenic insert for measurements in the thermal regime

In order to perform measurements at helium temperature, a cryogenic insert made up of diamagnetic steel has been realized. The top coverture presents three holes: two are for microwave cables and one has been made in order to supply the amplifier.
Two semi-rigid coaxial cables, named UT-085-SS. In Table 2.6 their charac-

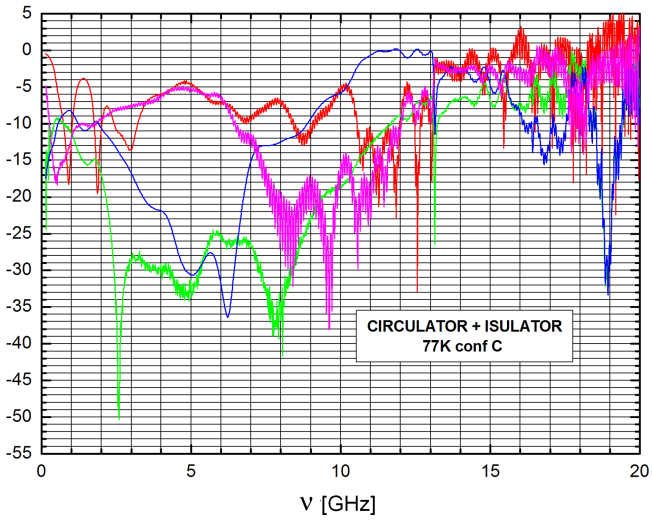

Figure 2.14: Measurements for the scheme including the circulator and the insulator at T=77K as a function of frequency ν. Here the transmission coefficient $\mathcal{S}_{31}$ (blue) is only 12 dB greater than other coefficients $\mathcal{S}_{11}$ (red), $\mathcal{S}_{33}$ (magenta) and $\mathcal{S}_{13}$ (green). Moreover it is possible to observe a great shift for all curves.

teristics are reported. In order to use them it was necessary to solder at the extremity two SMA connectors by Radiall(R.125.052.000).

A bifilar coax cable, realized by Axon S.A., has been used to connect the BNC to the amplifier. This cable has been chosen since it is essential to use a cable that presents a good electrical conductivity, but that doesn't heath too much the system. In the table 2.7 its characteristics are reported.

2.4 Measurements in the final configuration

At T=77 K, the calibration has been made considering the two microwave cables, the coax, and two final connections in order to realize transmission

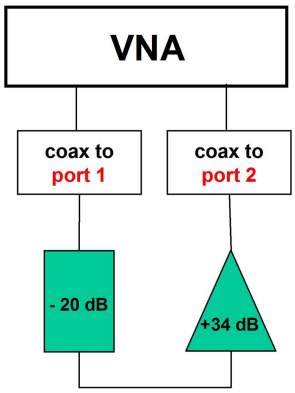

Figure 2.15: Picture of the scheme used to verify the cryogenic amplifier response. It was necessary to use an attenuator equal to -20 dB in order to consent to the VNA to read the output signal.

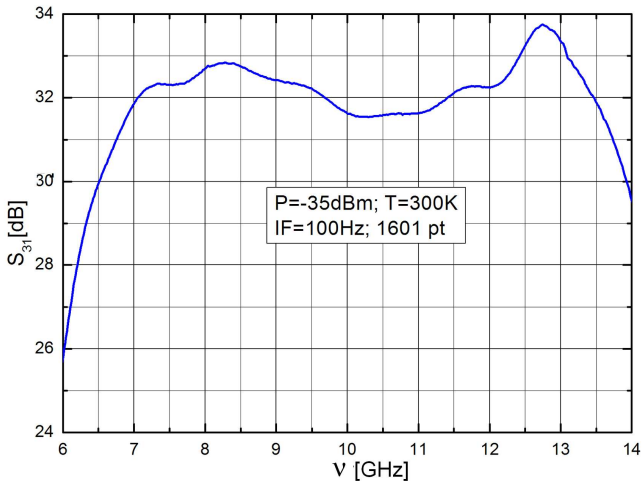

Figure 2.16: Measurement of amplifier response in the range 6 - 16 GHz. This measurement confirm the gain value declared on the datasheet and shows a good gain flatness in the range 8-12 GHz, where this amplifier is supposed to work.

measurements, while at T=4.2 K, the calibration has been made considering only the two microwave cable. For this reason measurements presented here

UT-085-SS coaxial cable	
Mechanical Characteristics	
outer conductor diameter (mm)	2.197±0.0254
dielectric diameter (mm)	1.676
center conductor diameter (mm)	0.511+/-0.0127
Minimum Inside Bend Radius (mm)	3.175
Weight (kg/100 meters)	1.86
Electrical Characteristics	
Impedance, ohms	50 ±1.0
Frequency Range GHz	DC-61
Velocity of Propagation (percentual)	70
Capacitance(pF/meter)	29
MATERIALS	
Outer Conductor	304 Stainless Steel
Dielectric	PVC Teflon
Center Conductor	SPCW

Table 2.6: Characteristics for the UT-085-SS coaxial cable.

AXON coaxial cable	
reference AXON	54552-001-3
diameter conductor (mm)	0.254
diameter core Teflon (mm)	0.80
diameter shield Mylar/aluminium-tape (mm)	0.90
diameter Jacket Teflon (mm)	1.1×1.35
impedance	50 Ω
capacitance	97 pF/m
resistance internal cable (copper)	0.36 Ω/m
resistance external cable and shield	0.27 Ω/m

Table 2.7: Characteristics for the Axon coax cable.

are not precise in phase, but this has no influence in studying the module of the reflection coefficient.

For low temperature measurements, the *configuration C* has been used. It has been realized with the two AEROTEK devices (since the AEROTEK circulator works better at low temperature). These measurements were performed by introducing also an attenuation equal to -40 dB, in order to study quantum phenomena, and the differential amplifier. The scheme used for measurements is illustrated in Fig.2.17.

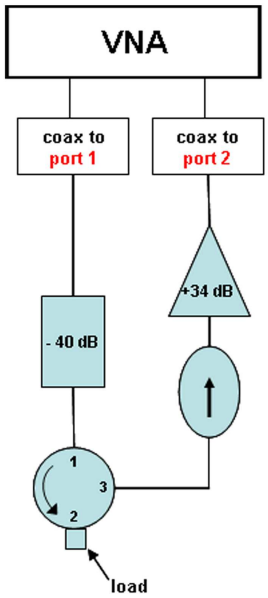

Figure 2.17: Schematics for measurements at low temperature including the circulator, the insulator, the attenuation and the cryogenic amplifier.

The short

First I studied the case the load is a short. Using this load all the input signal is transmitted from the port 1 to the port 3, and the loss are minimized.

Little oscillations that are visible on the graph related to $\mathcal{S}_{31}$ are due to the following formula for the impedance of a short

$$Z = jZ_0 \tan \beta\ell \tag{2.6}$$

Moreover is useful to remind that the reflection coefficient is $\Gamma_L = -1$.
This measurement allowed to achieve the maximum signal for the transmission with this setup.

The open-ended coax

As a second test I put on the port 3 an open ended coax which behavior is well known [24, 23].
In this case some little oscillations in $\mathcal{S}_{31}$ are visible. They are due to the impedance of a open-ended circuit, described by the following formula

$$Z = -jZ_0 \cot \beta\ell \tag{2.7}$$

Again is useful to remind the reflection coefficient is $\Gamma_L = 1$. These measurement has been performed to be compared with the ones realized with a load equal to a short. As attended, the result is comparable in module with the one obtained by using the short as load.

The 50 Ω termination

Finally, the same measurement has been repeated with a 50 Ω termination on the port 3. This measurement has been performed in order to establish the zero transmission threshold for this setup, since with a 50 Ω termination the signal should be completely adsorbed for an ideal termination.

In Fig.2.20 the module of the Γ_L coefficient is reported for the three different

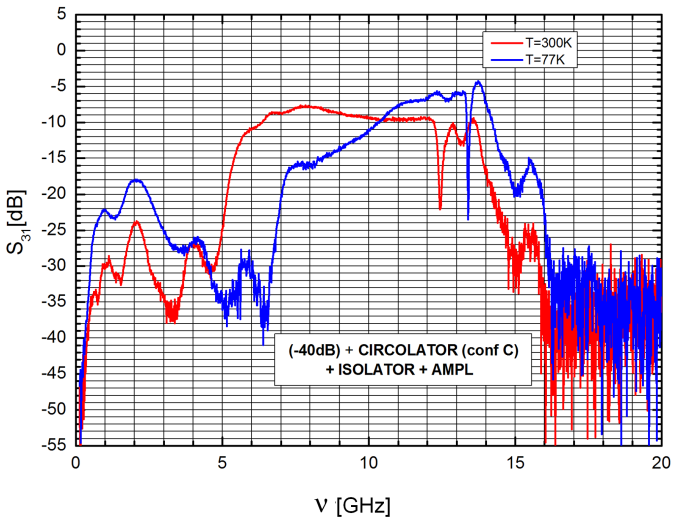

Figure 2.18: Measurement of $\mathcal{S}_{31}$ curve when the load is a short, for T=300K (red curve) and T=77K(blue curve) as a function of frequency ν. In this case the signal is maximum. As before it is evident a shift for the curve at lower temperature.

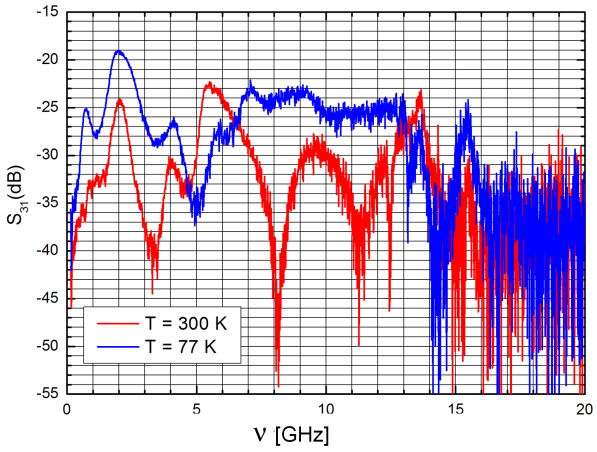

Figure 2.19: Measurement of $\mathcal{S}_{31}$ curve when the load is a 50Ω, for T=300K (red curve) and T=77K(blue curve) as a function of frequency ν. In this case the signal is minimum. As before it is evident a shift for the curve at lower temperature.

loads in this configuration.

The Γ_L value is always smaller than one, and this is due to the fact that

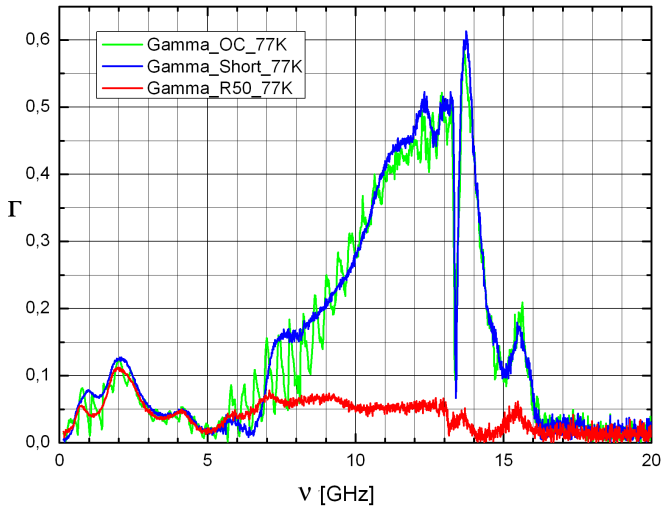

Figure 2.20: Measurement of the module of the Γ_L coefficient for the three different loads in *configuration C* as a function of frequency ν. It is possible to observe that Γ_L value is always smaller than one, and this is due to the fact that the devices are not ideal and present some losses.

the devices are not ideal, but present some losses.

Noise for *configuration C*

Finally a test to measure the noise that arrives as a reflected signal from the insulator to the circulator in *configuration C* has been made. In order to do this the scheme in Fig.[**?**] has been used:

The configuration is reversed with respect to port 1 and port 2 of the VNA because preliminary tests showed that the transmission $\mathcal{S}_{31}$ works better than $\mathcal{S}_{13}$. Even if I measured all the four parameters at T=300K and at T=77K,

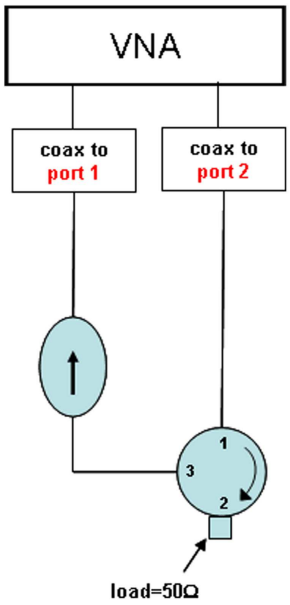

Figure 2.21: Scheme used in order to estimate the noise in the *configuration C*

but the only parameter interesting is the $\mathcal{S}_{31}$ curve. In Fig.2.22 noise values that arrive at the input of the cryogenic amplifier are reported. The red line ($\mathcal{S}_{31}$) at T=300K and the blue line is the transmitted signal at T=77K.

Measurements with a HP bandpass filter

Looking at measurements in *configuration C* it turns out that the noise could be due also to some frequencies external to the insulator bandwidth. So that it could be a good improvement to use a filter before sending the microwave signal to the amplifier. In order to verify this I performed a preliminary test with the bandpass filter HP 0955-0446 (from the calibration kit) which characteristic frequency is ν_0=10.24 GHz. I studied two different configurations, at T=300K and at T=77K.

First in *configuration FA* the filter is put just before the amplifier, as it is

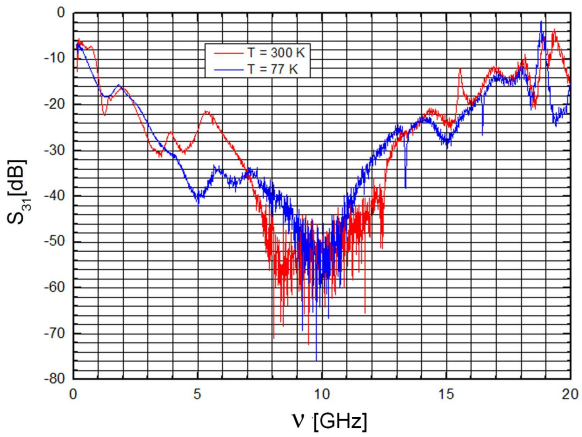

Figure 2.22: Measurement of the noise values for the transmitted signal as a function of frequency ν. This is the noise that arrives at the input of the cryogenic amplifier.

shown in Fig.2.23. In this configuration, it is interesting to look at the transmitted signal, that is the $\mathcal{S}_{31}$ curve.
Then I studied *configuration FB*, where the filter is used as an LC resonator on port 2 of the circulator, as shown in Fig.2.25.

For these measurements I first focalized on a smaller region with an higher sensitivity, so the calibration and measurements have been made with parameters reported in Table2.8:

Power	-65 dBm
bandwidth	9.74 GHz ÷ 10.74 GHz
IF filter	10 Hz
AVG	no average
no. of points	401

Table 2.8: Parameters used for the calibration and for the measurements of the final setup in the *configuration FB*.

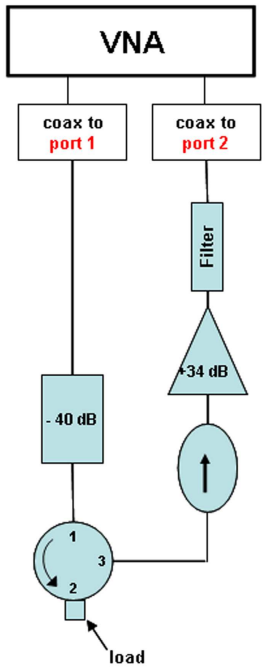

Figure 2.23: Scheme for Configuration FA

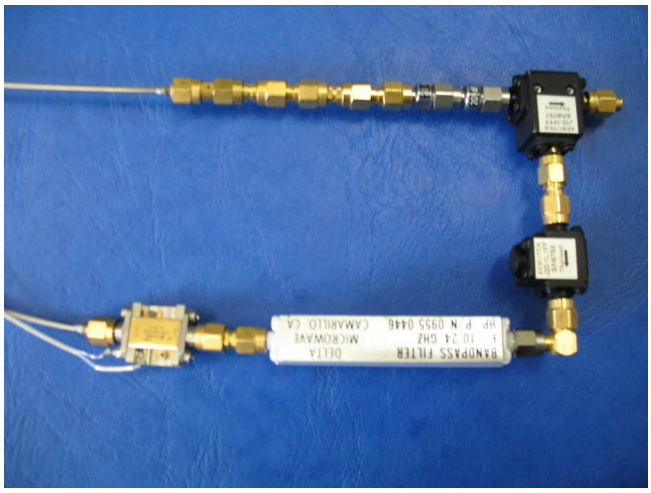

Figure 2.24: Realization for *Configuration FA*.

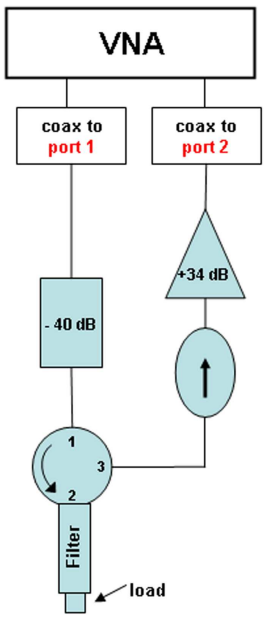

Figure 2.25: Configuration FB

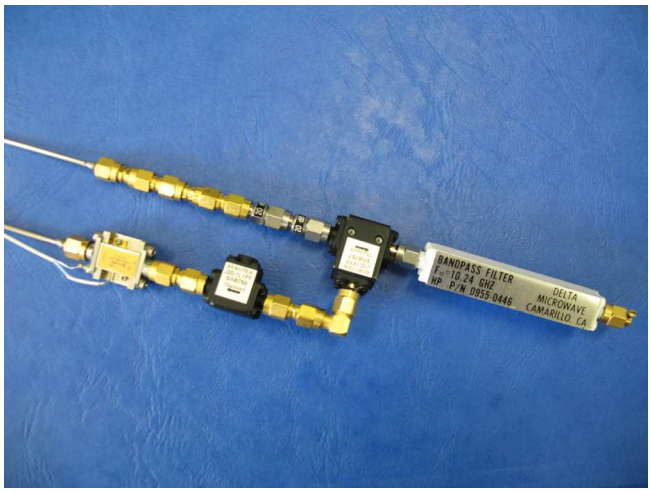

Figure 2.26: Realization for *configuration FB*

In Fig.2.27 it is shown the comparison of $\mathcal{S}_{31}$ curve when the load is equal to 50Ω and when the load is equal to a short. This display allows to evaluate

the minimum and the maximum for the transmitted signal.

In Fig.2.28 are reported the measurements at T=77 K, made with is the

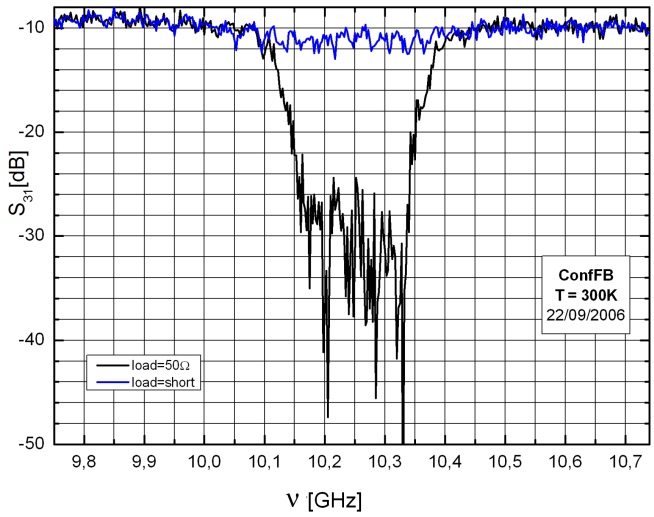

Figure 2.27: Comparison for a load equal to 50Ω and for a load is equal to a short at T=300K as a function of frequency ν for the *configuration FB*. In this case the difference between the two curves is about 20 dB.

same scheme. As for the single devices, it is evident that the behavior is worse at lower temperature.

I tested *configuration FB* also at T=4.2 K and the result is shown in Fig.2.29 where the same display described above is used.

The stronger attenuation in this case is due to the different calibration. Moreover it is evident that for T=4.2K is quite difficult to find a good working point. This is due to the anomalous behavior of the circulator at this temperature in the frequency range between 7 GHz and 11 GHz.

In fact the filter has been tested alone and it works as usual, even if the thermalization time is quite long.

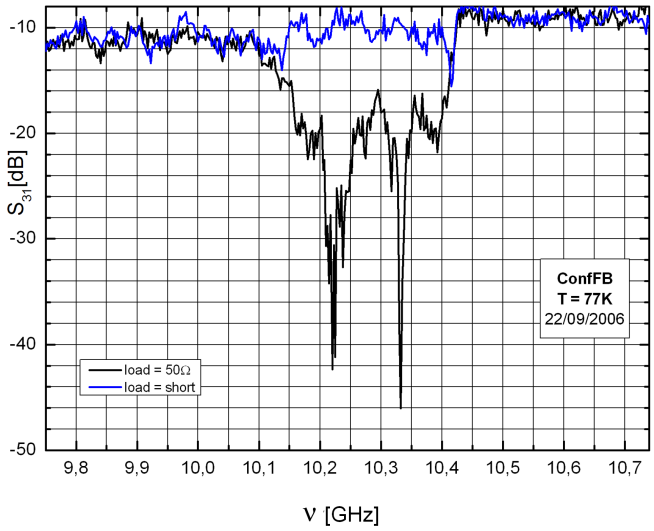

Figure 2.28: Comparison for a load equal to 50Ω and for a load is equal to a short at T=77K as a function of frequency ν for the *configuration FB*. In this case the difference between the two curves in some little range it is still equal to 30 dB, but in average it is about 10 dB.

2.5 Perspectives

As future improvement it could be useful to replace the insulator with another one having a larger bandwidth, because of the shift observed at low temperature. Moreover, in order to reduce the noise it could be useful to use also a bandpass filter, before the amplifier, like in *configuration FA*. In fact, by using this measurement setup, it should be possible to minimize the noise that starting from the amplifier is reflected and can reach the device. The insulator has a limited bandwidth, so that it is not able to filter the noise at higher frequencies.

Another improvement for future measurements could be to use a bandpass filter, centered on the bandpass frequency of the whole system, as in the *configuration FB*.

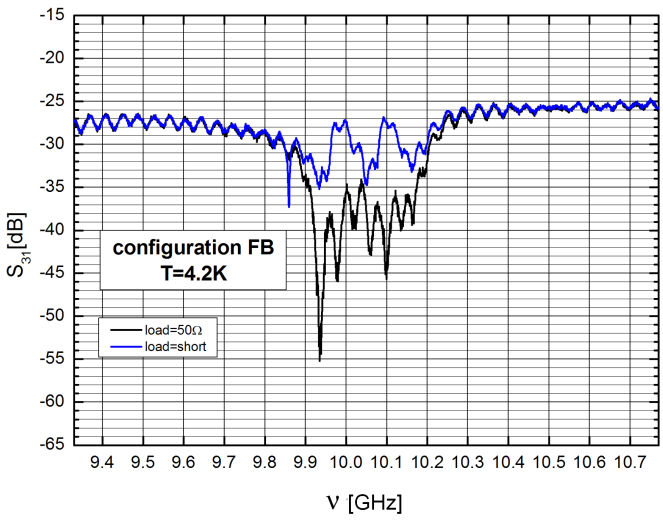

Figure 2.29: Comparison for a load equal to 50Ω and for a load is equal to a short at T=4.2K as a function of frequency ν for the *configuration FB*. In this case the difference between the two curves it is really too small.

Finally it could be useful to do a better evaluation of the noise for the final configuration. In fact, if G_n and F_n are respectively the power gain and the noise factor for the "n-th" element, the noise related to the total chain is expressed by the following formula:

$$F = F_1 + \frac{F_2 - 1}{G_{p_1}} + \frac{F_3 - 1}{G_{p_1} G_{p_2}} + ... + \frac{F_\ell - 1}{G_{p_1} G_{p_2} ... G_{p_{\ell-1}}} \tag{2.8}$$

so that it is evident that the first element, that is the circulator, should have an optimal noise figure, because its noise figure is determinant for the whole device noise figure.
Finally the thermal noise for the final setup has been estimated by using the formula

$$V_N = \sqrt{4 k_B T \Delta\nu R} \tag{2.9}$$

where $k_B = 1.38 \cdot 10^{-23}$ J/K, T=10 K, $\Delta\nu$=1 GHz, R=50Ω. By using these values I found V_N=5.25μV.

Chapter 3

Experiments on Josephson devices in presence of an external microwave excitation

In this chapter I describe the measurement setup and the related cryogenic apparatus, that have been especially developed for this experiment.
Mesoscopic effects, like Macroscopic Quantum Tunneling (MQT), typically occur on an energy scale of 1 meV or smaller. In order to measure these effects, experiments are usually performed at temperatures below 1 K in order to avoid thermal fluctuations. Such low temperatures are achieved with the help of cryogenic liquids with a very low boiling point (nitrogen and helium) and by using dilution cryostat.

3.1 The cryogenic insert

A cryogenic insert has been designed and realized to perform the preliminary measurements in the thermal regime (between 4.2 K and 1.2 K).
The cryogenic insert, shown in Fig.3.1, has been especially designed in or-

der to satisfy all the necessary requirements, such as vacuum tightness and feedthroughs for the high frequency signals. The cables used for this purpose are "Thermocoax cables" that allow to filter noise at frequencies above 1 GHz (a complete description of these cables is provided in section 3.2).

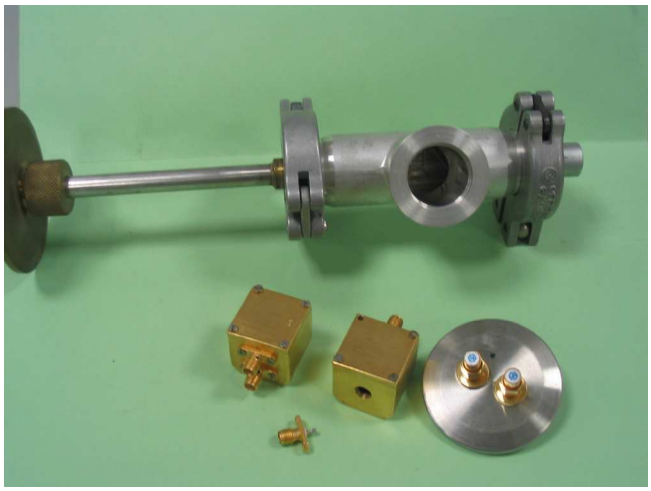

Figure 3.1: A detail of the cryogenic insert especially designed for this experiment.

Moreover, in order to perform measurements, it has been necessary to pass through the cryogenic insert also all necessary lines to bias both: a Josephson junction and a SQUID. I used 16 wires: 10 manganine wires (with a resistivity $0.43{\cdot}10^{-6}\Omega$m) and 3 twisted cooper pairs (with a resistivity $0.017{\cdot}10^{-6}\Omega$m). To reduce the electronic noise, different stages for the filtering have been realized at different temperatures. The filtering is the same for all the wires.

3.2 Special filtering cables: the thermocoaxes

Significant experiments investigating macroscopic quantum effects in Josephson systems have been performed by measuring the decay of the metastable state or the charge transfer [25, 26]. As well known the supercurrent decay

from the zero voltage state in a Josephson junction is strongly influenced by the dissipation and the inevitable coupling to electromagnetic environment. Various noise reduction techniques based on special dissipative coaxial cables have been investigated.
In order to study quantum effects it is necessary to avoid that the noise cover such effects. This means that the electrical lines to supply and read the device have to be filtered.
The filters have to work at different cryogenic temperatures and it is really important how the thermal anchorage is realized at each temperature, on the "plateau", since a good thermalization can minimize the noise that themselves generate. But in order to avoid the noise coming from higher temperatures and realize an effective filter, it is necessary to

- have a large band spectrum, MHz to 20 GHz in our case

- have a good thermalization.

The electrical lines should be such that the attenuation is exponential at high frequencies. If T is the sample temperature and T_s the noise source temperature, then the attenuation can be calculated by using the formula

$$A(\omega) = \frac{\exp(\hbar\omega/k_B T_S) - 1}{\exp(\hbar\omega/k_B T) - 1} \tag{3.1}$$

This means that if the sample temperature is 20 mK , the microwave frequency is 20 GHz and the noise temperature is equal to 1 K, the attenuation should be about -220dB. At higher frequencies the attenuation should be exponentially higher. This can be realized by using a dissipative coaxial cable. The principal transmission modes are the Trasversal Electromagnetic Mode (TEM).
If R is the resistance, C is the capacitance, L is the inductance, and $Z_c = (L/C)^{1/2}$ is the characteristic impedance of the coaxial cable and if we consider a frequency range such that $L \gg R$ and $R \gg Z_c$, then the attenuation A

of the TEM modes is expressed by the relation A=exp(-R/Z_c). By using eq.(3.1) it turns out that in order to have an attenuation equal to 200 dB we need R=2.3 kΩ with Z_C=50 Ω. But this resistance value is too high for normal commercial lines. Since the final goal is to obtain an attenuation exponentially growing with frequency, it's useful to use the skin effect. Over the characteristic frequency ω_c due to the geometry of the internal conductor of a coaxial cable with $R(\omega) = R_{dc}(\omega/\omega_c)^{1/2}$ where R_{dc} is the dc resistance; so that

$$A(\omega) \simeq \exp(-\sqrt{\omega/\omega_c}R_{dc}/Z_{dc}) \tag{3.2}$$

In this experiment we utilized the triaxal thermocoaxes where the inner conductor is made of manganina with a diameter equal to 0.127 mm and resistivity 34 Ω/m at 4.2 K, while the insulator is made up of a formvar sheet with a thickness equal to 22 μm. These conductors are placed inside a steel diamagnetic can with an internal diameter equal to 820 μm and external diameter 1.2 mm, fixed with a silicon glue.
Thermocoaxes cables are intended for signal transmission at high frequency [27, 25]. Two types have been developed:

- coaxial cable with composite shielding: an iron layer in the shielding reduces the transfer impedance of cable.

- triaxial cable: this is a coaxial cable with a supplementary sheath by which the cable is insulated from the ground.

The level of protection is given by the transfer impedance of the cable i.e. by the ratio between the signal voltage picked up by the central wire and the current flowing on the outer shield. For a weaker impedance, a better protection from interface is obtained.

3.3 The sample holder

The sample holder, shown in the Fig.3.2, has been especially designed for this experiment. It has been realized in cooper in order to guarantee an optimal thermalization at low temperatures. The cavity has been obtained by milling a piece of bulk cooper. The measures of the cavity are: 22mm x 22mm x 11mm.

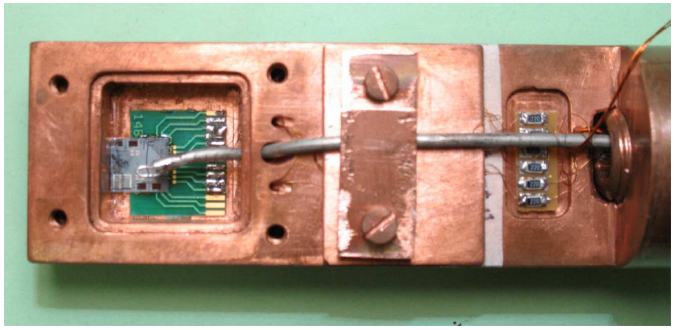

Figure 3.2: Picture of the sample holder that has been designed and realized especially for this experiment.

The cavity is closed by a cover realized in copper and an indium seal is used to guarantee the perfect matching between the cavity and the cover, in order to minimize the losses and ensure that the cavity is screened against RF radiation.
The filtering on the sample holder has been realized accurately, since the final goal is to study quantum phenomena in Josephson based devices, that are really sensitive to electromagnetic noise. This sample holder has been designed so that it can also be used in the dilution cryostat.
In order to study the cavity I have performed some preliminary measurements at T=300K and at T=77K to archive the spectrum of the cavity by reflection measurements. In Fig.3.3 a detail of results obtained for this study

is reported. As expected, it's possible to observe a shift in the spectrum due to the small change in dimensions of the cavity at lower temperature.
The knowledge of the cavity resonance frequencies is extremely useful in order to avoid them in experiment with Josephson devices.

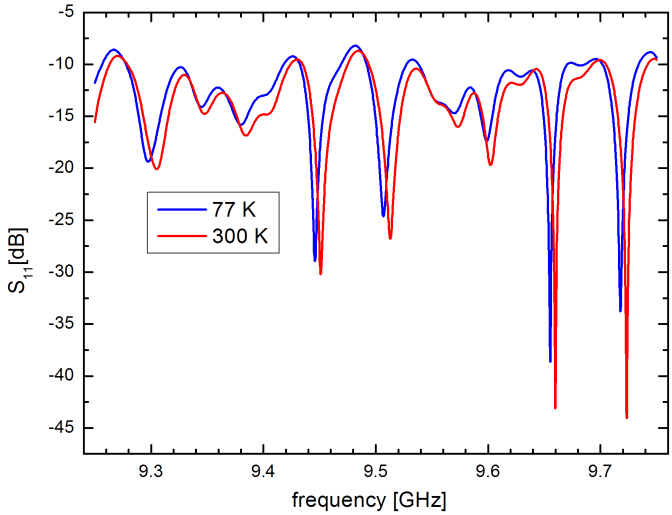

Figure 3.3: A detail of measurements to evaluate the spectrum of the cavity at T=300K (red line) and at T=77K (blue line). Below 77K the spectrum is practically the same.

In order to bias the junction, 22 Ω limiting resistors have been used.

3.4 Electronic setup for the Josephson junction

Measurements described in this chapter have been performed by using a low noise electronic especially designed at ICIB-CNR [27]. This electronics allows to measure the I-V characteristic by biasing the junction with a current I_b and

measuring the drop-voltage V by using a four-contacts technique. With this technique it is possible to decouple the wires for the bias from the wires for the voltage, so that the resistance value for the measured device is obtained without considering the wires contribution. The electrical scheme for the device is reported in Fig.3.4.

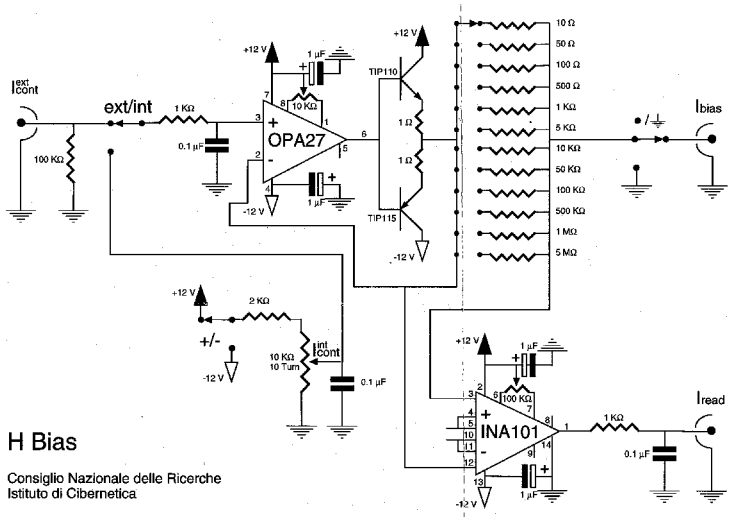

Figure 3.4: Picture of the electrical scheme for the device that allows to measure the I-V characteristic for the Josephson junction.

The junction is biased by using a triangular shape current with a frequency equal to 200Hz. This current is amplified by using a differential amplifier OPA, having a low noise figure and a gain equal to one. Then the bias current, flows through a shunt resistance R_{shunt} that can vary from 100 Ω up to 100kΩ, having an high precision (dR_{shunt}/R_{shunt}=0.01).
The current that flows through the junction, I_{read}, is measured by taking the voltage V_{shunt} on the shunt resistance and sending it to an amplifier with a gain equal to one and precision 1%. So I_{read} is simply obtained by applying

the Ohm law

$$I_{read} = \frac{V_{shunt}}{R_{shunt}} \tag{3.3}$$

In order to read the voltage drop for the junction two stages are used: the first one has a gain equal to 5, the second one has a gain equal to 5.2. So the voltage drop is finally amplified 26 times. Moreover there is a switch "short-open" in order to decouple the junction and the readout electronics. The voltage and the current are sent, respectively, to the X and Y channel of a oscilloscope Tektronix TDS 620B.

3.5 Measurement scheme for a test Josephson junction

The synchronism of the ramp generator is delayed and sent to the start input of a time-to-amplitude converter (TAC). The junction voltage is amplified and sent to a discriminator that provides the stop signal for the TAC at the time of the switching out of the V=0 state. The TAC then provides a voltage signal, proportional to the time elapsed between the start and the stop input, that is sent to an analog to digital converter. With this setup a count is assigned to the channel corresponding to the switching time. About 45.000 events were recorded to get the experimental histograms equivalent to the switching time distributions. Time scale of the TAC can be set starting from a minimum of 9 ps/channel up to 360 ns/channel. After each set of measurements the current ramp has been measured to get dI/dt, which multiplied for TAC time scale Δt gives the current resolution 5$\div$10 nA/channel. The obtained P(I) is then related to the escape rate out of the V=0 state Γ(I) by the equation

$$P(I) = \frac{dt}{dI}\Gamma(I)\exp\left[-\int_0^I (\frac{dt}{dI'}\Gamma(I)dI'\right] \tag{3.4}$$

The measurement scheme, shown in Fig.3.5, assures a very low noise level. Data have been recorded by using a multichannel system and have been stored as histograms showing the number of counts P(K) in the channel K. We then associate a current I(K) to channel K by using the calibrated time interval per channel and the measured current sweep rate dI/dt to determine the current interval per channel, denoted as ΔI, as well as the measured current corresponding to the first channel I(t = 0).

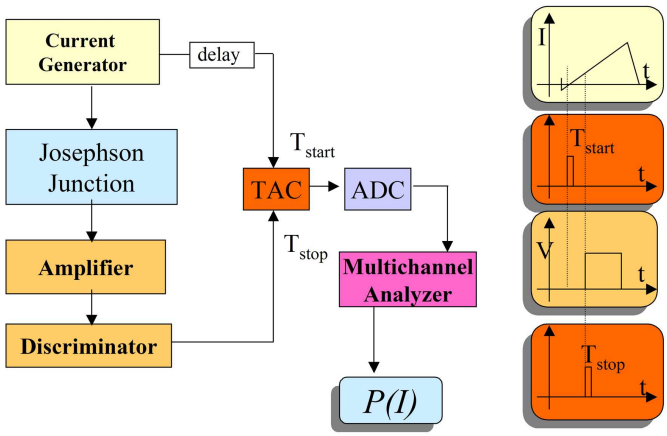

Figure 3.5: The measurement scheme used to measure and characterize the Josephson junction.

Here K_{max} is the channel corresponding to the highest value of the switching current. From the measured histograms the escape rate Γ is computed [28] according to the formula:

$$\Gamma(K) = \frac{dI}{dt}\frac{1}{\Delta I}\frac{P(K)}{\sum_{j=1}^{K_{max}} P(j) - \sum_{j=1}^{K} P(j)} \tag{3.5}$$

where ΔI is the channel width of the analog-to-digital converter.
For these measurements high quality Nb-AlO_x-Nb Josephson tunnel junctions, fabricated at the ICIB-Istituto di Cibernetica "E.Caianiello" of CNR

in Naples, have been employed. The devices exhibit a very low leakage current and a quite uniform critical current density J_c=9.0±0.4 A/cm^2. This value is low enough to obtain an extremely low dissipation level. The area is A =5·5 μm^2, the capacitance is C=2.3±0.2 pF, as measured from the Fiske step voltage and using the penetration depth of Nb film (obtained from the magnetic field diffraction pattern) [17], while L_0 = 0.39±0.4nH. These measurements allows to evaluate the critical current that is I_c=58±2μA.

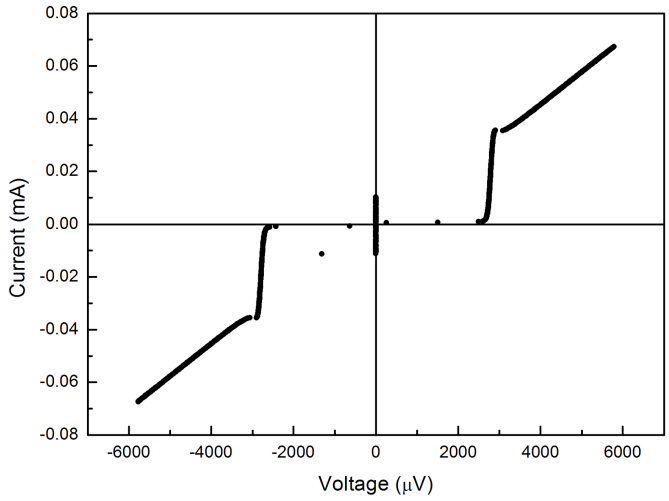

Figure 3.6: Measurement of the I-V characteristic for the Josephson junction is reported. The designed dimension for this junction was 5×5μm^2. The measured parameters are L_0 = 0.39±0.4nH, C=2.3±0.2 pF.

The quasiparticle resistance R_{qp} [A.3] at zero bias has been measured by the application of a small magnetic field to suppress the dc Josephson current. It depends exponentially on the temperature and this leads to a very low intrinsic damping level at low temperatures.
It is worth stressing that the effective resistance [A.3] in this kind of experiment may be limited by external shunting impedance. For these measure-

ments 22 Ω shunt resistors located close to the junction have been used and while great care has been devoted to avoid stray capacitance, which might reduce the real part of the complex impedance at the junction plasma frequency, which at zero bias is about 16.9 GHz, as verified by the means of a VNA.

3.6 The ^{4}He cryogenic system

All measurements in the thermal regime presented here have been performed by using a ^{4}He cryostat. It consists of a shielded dewar and a pumping system that, by extracting helium vapors, allows to reach temperatures lower than liquid helium temperature (4.2 K). In fact such a system allows to go down to 1.15 K by using a pressure equal to 1 Torr ($1.28{\cdot}10^{-3}$atm).

Figure 3.7: The shielded dewar used for measurements in the thermal regime.

Inside the dewar there is a shield realized with two diamagnetic steel layers, such that in the middle is possible to obtain a pressure equal to 10^{-4} Torr, that guarantees an optimal thermal isolation.
The internal side of the cryostat is covered by *mylar* sheets, a material that presents an high reflectivity that allows to minimize the heating of the internal surfaces due to the radiation effect.
When helium is present between the two diamagnetic steel layers, the pressure goes down to 10^{-7} Torr, and a better thermal isolation is achieved. Moreover, in order to avoid the effects of external electromagnetic fields on the Josephson current, inside the dewar there is a shielding system made up of five cilindric shields, two in copper and three in μ-metal. The copper shields the high frequency electromagnetical fields while the μ-metal, that presents an high permeability, shields the static and low-frequency fields.
The pumping system consists of a Roots pump, with a rate equal to 350 m^3/hour, coupled to a rotative pump, with a rate equal to 35 m^3/hour.
The pressure inside the cryostat can be controlled and varied in the range $760 \div 40$ mmHg with a precision equal to 0.5 mmHg, that corresponds to some mK. When the pressure is equal to 40 mmHg the temperature inside the dewar is 2.2 K, that is the temperature at which the transition to the superfluid state happens.
It's possible to reach lower temperatures by using a low impedance line, but it's worth noting that below 2.2 K is not possible to control the pumping rate, so that is difficult to archive a fine control on the pressure and, as a consequence, on the temperature.

3.7 Measurements in the thermal regime for the Josephson junction

Measurements in the thermal regime for the Josephson junction have been performed in the ^{4}He cryogenic system.
The junction has been biased through a 100 kΩ resistor with a triangular-shaped wave form, whit amplitude V_{pp}=4.70 V. Moreover the junction has been excited by using a microwave generator. I explored a large interval of frequencies, ranging from 13.00 GHz up to 18.00 GHz, with a span equal to 200MHz, in order to find the resonance related to macroscopic tunneling phenomena.
The junction has been supplied with following values:

ΔV_{ampl}	frequency	offset	delay	width	leadge
4.60 V	200 Hz	-2.0 V	1.73 ms	10 μs	100 ns

Table 3.1: Values used to supply the Josephson junction.

The switching current distributions have been measured by a fly time technique (details are reported in Refs.[29, 30]).
The first experimental goal has been to characterize the sample under a continuous microwave excitation at different temperatures. In order to do this the transition probability from one metastable state to another one has been studied. In Fig.3.8 rate escapes measured at different temperatures are reported.
In these measurements the escape rate Γ from the zero voltage state of the junction was determined using the method described in section 3.5 (details are reported in [28]). So the bias current has been increased until the switching to a non-zero voltage is observed for the Josephson junction. This voltage gives the start signal to an Analog-to-Digital converter that allows to monitor the current, so that is possible to obtain the value of current at which

the junction switched. By repeating this procedure a large number of times, typically 10^4, it is possible to obtain the distribution of the switching currents P(I). The escape rate is then evaluate according to the formula [28]

$$\Gamma(I) = \frac{P(I)dI/dt}{1 - \int_0^I P(i)di} \tag{3.6}$$

In resonant activation [31, 32, 33] it's measured the escape rate Γ of the zero voltage state of the junction in the presence of a microwave power P. The microwave current produces a sinusoidal force on the particle, so that it's possible to observe an enhancement in the escape rate of the metastable state when the microwave frequency is close to the plasma frequency. If the behavior of the "particle" in the potential well is determined by quantum mechanics, then the particle energy should be quantized. To investigate this behavior, measurements were performed in the quantum regime for the Josephson junction. In this case, the action of microwave power should be to enhance the escape rate when the frequency coincides with the spacing between two energy levels.

The escape rate Γ has been measured at a fixed value of bias current for different values of the microwave frequency and each set of measurements was repeated at different temperatures.
In order to study the phenomena it's better to display the $\log[\Gamma(P)/\Gamma(0)]$.
It is worth noting that microwave current used for these experiments is very small so that it induces only a minor perturbation on the dynamics of the junction in the presence of thermal noise.

In these experiments the microwave power has been chosen such that $[\Gamma(P) - \Gamma(0)]/\Gamma(0) \leq 2$. In the Fig.3.10 is reported the $ln[\Gamma(P)/\Gamma(0)]$ vs. the microwave frequency. The observed peaks provide further information on junc-

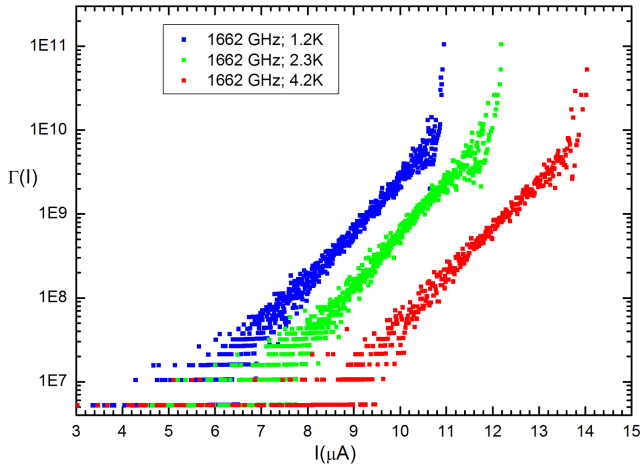

Figure 3.8: Measurements of the escape rate Γ measured for a fixed value of bias current and a microwave frequency equal to 16.62 GHz. Measurements are shown for different temperatures.

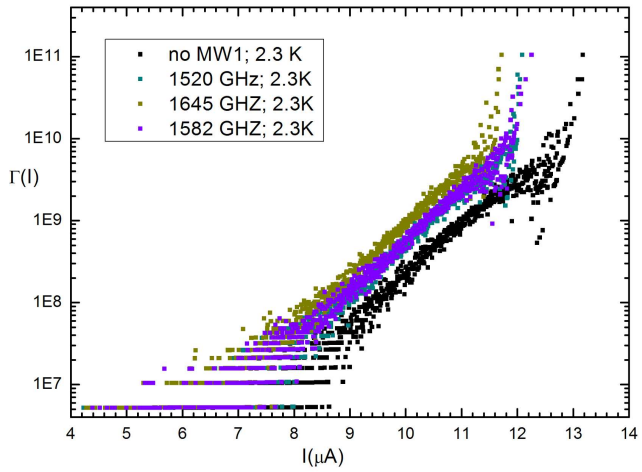

Figure 3.9: The escape rate Γ has been measured at T=2.3 K, for a fixed value of bias current and for different values of the microwave frequency and they are compared with the escape rate measured without microwave.

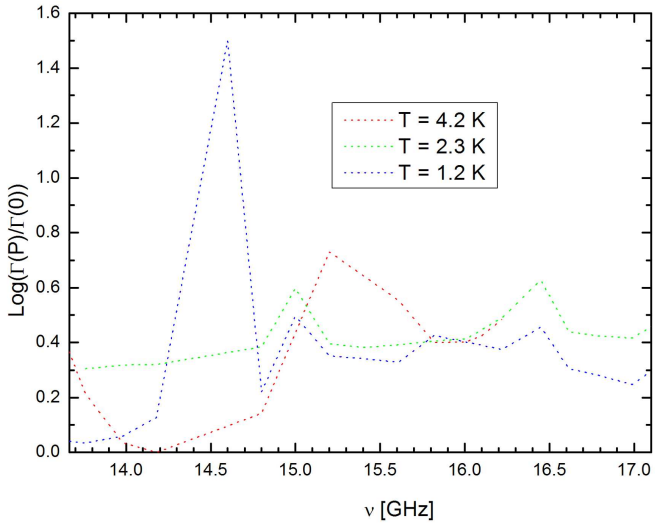

Figure 3.10: Experimental data of escape rates $\log[\Gamma(P)/\Gamma(0)]$ vs. microwave frequency ν. The data refer to different temperatures.

tion parameters and characteristics.

At lower temperature peaks in the escape rate can be observed when the spacing between the ground state and the excited state coincide with the microwave frequency. This means the microwave let the particle to go from the ground state to the excited state, in which the lifetime against tunneling out of the well is substantially reduced. At values $k_B T/\hbar\omega$ such that there is a significant population of the lower excited states, transitions between different energy levels have been observed.

By applying a bias current slightly lower than the critical current I_0 it's possible to prepare the particle in a local minimum of the tilted cosine potential. In this metastable state, under the influence of the thermal and microwave currents, the particle oscillates around a minimum value and the junction is in he zero-voltage state. Moreover here I consider only the case of junction with an hysteretic I-V characteristic ($2\pi I_0 R^2 C \gg \Phi_0$) in which the damping is sufficiently low that the particle is never trapped in another well after

escaping from the initial metastable state. So, in these conditions, after escaping the particle runs freely down the tilted cosine potential.
In the absence of a driving microwave current ($\mathcal{I}$=0) the escape of the particle occurs via thermal activation over the barrier or via quantum tunneling through the barrier.
The $\ln\gamma$ strongly depends on three parameters: the temperature, the frequency and amplitude of the microwave current.
When a weak microwave current is applied to a current biased Josephson junction in the thermal limit the escape rate from the zero voltage state is enhanced when the microwave frequency is near the plasma frequency of the junction.

3.8 Basic measurements on final Josephson devices

Here I present some configurations for SQUID-based devices that have been designed in order to study MQT effects.
I present also measurements that have been performed on these devices in thermal and quantum regime. In fact it is important, as first step, to test the correct behavior of the device in absence of a microwave signal, in order to gather information on the design parameters.

3.8.1 Devices design: the scheme

In this section geometrical configurations for the whole device is described.
As shown in Fig.3.11, it contains an rf SQUID and a readout system based on a dc SQUID sensor, coupled to the probe through a superconductive flux transformer. The design allows also the possibility to reduce drastically the coupling between the probe and the readout system by means of an injection

current in a stacked Josephson junction [34] , or the flux modulation of a vertical josephson interferometer [35, 36, 37] inserted in the flux transformer. The quantum state of the rf SQUID is controlled by an external magnetic flux, provided by a niobium single coil located inside the rf SQUID loop.

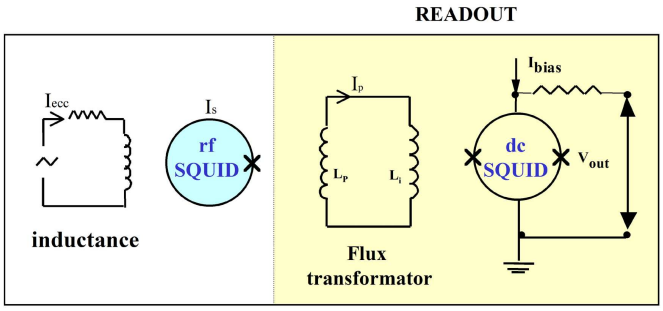

Figure 3.11: The scheme of the rf SQUID-based device.

When an increasing excitation flux is applied, a screening current flows in the superconducting ring until the value of the critical current of the Josephson junction is reached; then a flux quantum penetrates the loop [A.1]. The readout system is made up of a dc SQUID amplifier and a flux transformer. Moreover, a single niobium coil for the modulation of the dc SQUID is integrated in the device and it can be used also to compensate the magnetic signal produced by the excitation coil. Finally thin film gold-palladium resistors have been inserted across all coils to realize integrated filtering stages. Thin AuPd film resistors have been inserted across all coils to realize rf integrated filtering stages and a damping AuPd resistor (R_d=2.5Ω) has been inserted across the dc SQUID inductance to improve the performances of the reading device.

Different configurations of SQUID based devices, designed according to the scheme presented above, have been realized and two of them, with a diffe-

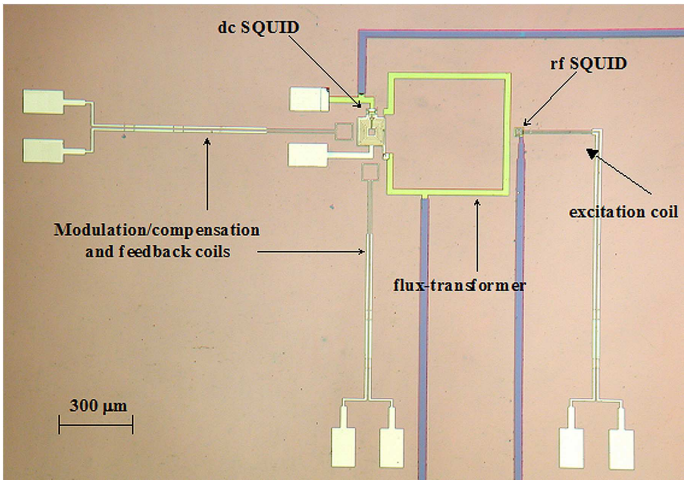

Figure 3.12: Picture of a SQUID-based device: configuration with a magnetometric readout.

rent readout system, appeared extremely interesting. They are illustrated in Fig.3.12 and Fig.3.13.

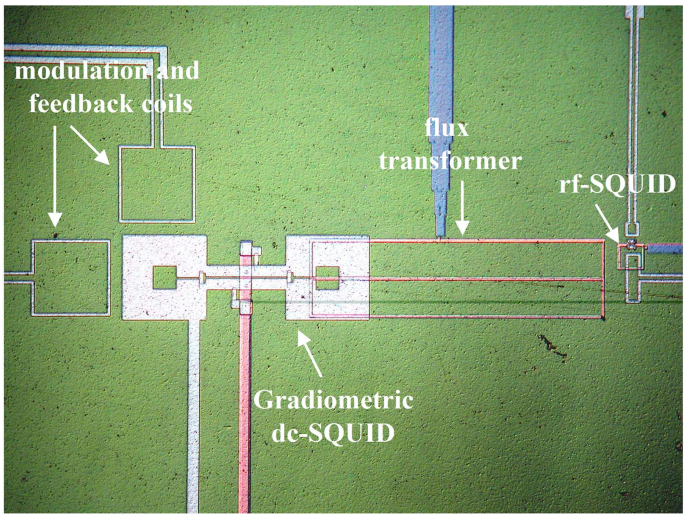

Figure 3.13: Picture of SQUID-based device: configuration with a gradiometric readout.

3.8.2 Measurement scheme

When the rf SQUID parameter β_L [eq.A.5] is greater than one, the system is described by a multi-well potential, corresponding to different metastable states (flux states) of the rf SQUID [A.1]. In order to evaluate the intrinsic dissipation of our system transitions between adjacent flux states of the rf SQUID, as a function of the external flux Φ_x, have been measured. If noise level is low enough, the escape from the metastable state should occur at a critical value of the external flux Φ_{xc}. Quantum tunneling as well as thermal noise, induce transitions at random values of Φ_x smaller than a critical value Φ_{xc}, whose probability distribution, $P(\Phi_x)$, has been measured.
Data have been collected by standard fly time technique that has already been described earlier in this chapter. The measurement scheme is the same presented in Fig.3.5, but the Josephson junction is replaced by a rf SQUID, so that the measured quantity is a $P(\Phi_x)$. The only difference with respect to the scheme presented in Fig.3.5 is that in this case it is necessary to measure the quantity τ_0, i.e. the time interval corresponding to a change of a flux quantum Φ_0 in the rf SQUID and is measured experimentally on the oscilloscope. In this way experimental histograms are then converted into functions of the external flux following the normalization:

$$K \rightarrow K\Delta t \frac{2\pi}{\Delta\tau_0} \tag{3.7}$$

3.8.3 Decay from metastable states in SQUID-based devices

If external sources of noise are filtered out, the intrinsic dissipation of the Josephson junction is due to the tunneling of thermally activated quasiparti-

cles [A.3], and it is strongly decreasing with decreasing temperature. In this section experimental data on the effective dissipation for the fully integrated SQUID-based devices described before, are presented.
Results have been obtained by studying the escape process from the metastable flux states as a function of the external flux Φ_x, at different temperature values.

3.9 Experimental results for SQUID-based devices in the thermal regime

First I have performed measurements in thermal regime to archive configurations that present a lower dissipation level, that is an higher effective resistance. The value of R_{eff} [A.3] is obtained by fitting experimental data with Buttiker-Harris-Landauer (BHL) theory [38], that predicts an exponential behavior of the escape rate Γ_t:

$$\Gamma_t = A_t \frac{\omega_0}{2\pi} \exp\left(-\frac{\Delta U(\Phi_x)}{k_B T}\right) \tag{3.8}$$

where

$$A_t = \frac{4}{\left[1 + \left(1 + \frac{k_B T}{\Delta U(\Phi_x} \frac{\omega_0 RC}{1.8}\right)^{1/2}\right]^2} \tag{3.9}$$

ΔU is the height of the rf SQUID potential energy barrier and ω_0 is the plasma frequency defined as

$$\omega_0 = \left[\frac{1}{C(\Phi_0/2\pi)^2}\left(\frac{\partial^2 U(\Phi_{min})}{\partial \Phi^2}\right)\right]^{1/2} = \left[\frac{1}{LC}(1 - \beta \cos \Phi_{min})\right]^{1/2} \tag{3.10}$$

where Φ_{min} is the flux corresponding to the minimum value for the potential $U(\Phi)$.
Theoretical behavior of the switching flux distribution $P(\Phi_x)$ is derived from

the expression of the escape rate:

$$P(\Phi_x) = \Gamma(\Phi_x)\frac{\Delta\tau_0}{2\pi}\exp\left[-\int_0^{\Phi_x(t)}\Gamma(\Phi_x)\frac{\Delta\tau_0}{2\pi}d\Phi_x\right] \tag{3.11}$$

Actually the BHL formula is an extension of the older Kramers theory [39], which provides two different expressions for the escape rate in the moderate and extremely low damping regime respectively. Moreover the BHL theory introduces a prefactor which smoothly connects the two regions.
A further fitting parameter that can be obtained by theoretical analysis, is the noise temperature T_N, that takes into account the presence of a spurious noise. In the ideal case, the effective temperature of the sample should be coincident with the bath temperature T_b, measured by a thermometer placed on the mixing chamber. In real cases external noise is not negligible, so that the effective temperature T can be expressed as the sum of two terms: $T=T_b+T_N$.
Since R_{eff} and T_N are correlated, in order to analyze experimental data it's necessary to elaborate a consistent number of histograms, collected at different temperatures, since the analysis of a single probability distribution can only give order of magnitude for fitting variables.
All the other rf SQUID parameters, such as C, I_c, β_L, as well as the bath temperature T_b, are independently measured, and they are fixed thanks to fitting procedure.

A first measurement has been performed at T=4.2 K on the sample having a magnetometric configuration, presented in Fig.3.12. In Fig.3.14, the switching probability distribution and the escape rate of the rf SQUID as a function of the external flux Φ_x are reported.
For this configuration and these parameters, the effective resistance R_{eff} is 300Ω, corresponding to a Q factor of 10^2. Within the experimental uncertainty (about 100 mK) of the fitting procedure, the temperature T is

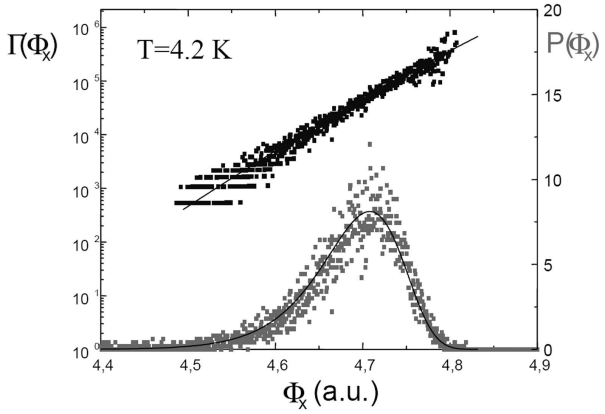

Figure 3.14: Sample in magnetometric configuration: switching flux distribution $P(\Phi_x)$ and escape rate $\Gamma(\Phi_x)$ (dots) of the rf SQUID as a function of the external flux at T=4.2 K. The solid line is the theoretical prediction within the BHL theory (L=80 pH, C=2.3 pF, I_c=30.0μA, R_{eff}=300Ω.

consistent with the bath temperature T_b.

The same measurement has been repeated for the second configuration, having a gradiometric read-out system. The noise temperature is still negligible, but the value of R_{eff} is of the order of the kilo-ohm, corresponding to a Q factor of 10^4. This result confirms that the gradiometric configuration is better decoupled from external environment and, as a consequence, it has been selected for measurements in a wider temperature range. In Fig.3.15 the switching flux distribution $P(\Phi_x)$ of the rf SQUID is reported as a function of the external flux Φ_x at different temperatures. As attended, at lower temperature distributions are more enhanced.
The time interval $\Delta\tau_0$, corresponding to a flux quantum Φ_0, has been experimentally measured and ranges between 1.1 ms and 1.8 ms. In the Fig.3.15 theoretical curves are obtained with the BHL theory in the extremely-low-damping limit, with L = 80 pH, C = 2.3 pF, I_c = 15.0μA. Noise temperature

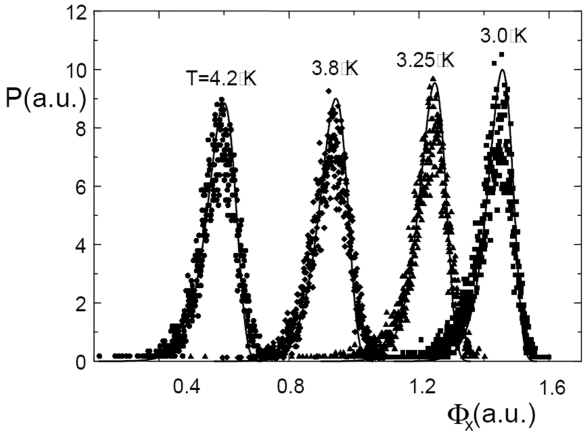

Figure 3.15: Sample in gradiometric configuration: experimental data (dots) and theoretical predictions (solid line) of the switching flux distribution $P(\Phi_x)$ at different temperatures. The common fitting parameters are: L = 80 pH, C = 2.3 pF, I_c=15.0μA, β_L= 3.3.

T_N <100mK indicates the effectiveness of integrated filters in reducing the external noise. The Q factor obtained from data at different temperatures is exponentially increasing, since the resistance R is determined by tunnelling of thermally activated quasiparticles, as confirmed by the exponential fit shown in Fig.3.16.
The resistance behavior is described by the law

$$R = R_0 \exp(\Delta / k_B T) \tag{3.12}$$

By fitting data, we obtained R_0=109 Ω and Δ=1.33 meV, which reasonably fits the niobium gap energy of 1.25 meV for thin films [40]. It's worth noting that the dissipation level is really low, comparable with the intrinsic one.

For these two configurations, we performed measurements in quantum regime

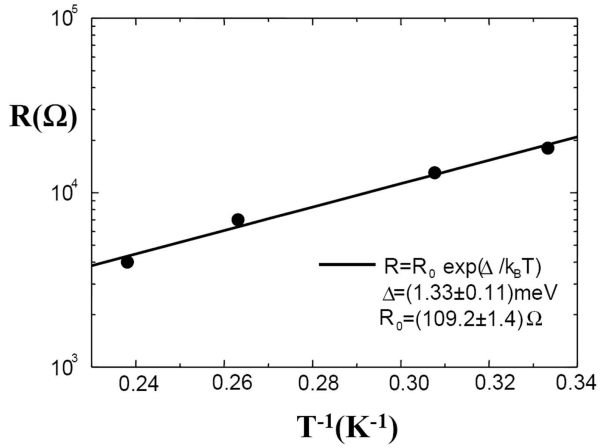

Figure 3.16: Fitting resistance R as a function of the inverse of the temperature. The effective resistance increases exponentially with decreasing temperature, R=R$_0$ exp(Δ/k_BT). This behavior shows that the dissipation mechanism is essentially due to the tunneling of thermally activated quasiparticles of the Josephson junction. R$_0$=109 Ω and Δ=1.33 meV.

3.10 The ^{3}He/ ^{4}He dilution cryostat

All these measurements were performed in a ^{3}He/ ^{4}He Oxford dilution cryostat having a base temperature of 20 mK. Several copper, aluminum and μ-metal magnetic shielding have been included in order to shield the sample from external magnetic fields.

A diamagnetic ceramic (shapal) mounting, screwed to the mixing chamber, has been especially designed for the experiment. The shapal is a machinable material with high mechanical strength and thermal conductivity (90 W/mK), based on translucent aluminium nitride ceramic. Since it is diamagnetic it guarantees a lower noise noise in SQUID measurements.

The chip is glued on a 0.4 mm thin vetronite film provided of gold paths. Thermal contact between the sample and the shapal mounting is obtained through a small hole in the vetronite chip carrier, filled with a special low

temperature grease (Apiezon N).
The sample is electrically connected to the chip carrier through aluminum bondings. NbTi wires are then soldered on gold pads present on the vetronite film. These wires are carefully thermalized through copper pegs from mixing chamber to 4.2 K stage. Then, crimped Nb small tubes guarantee a superconducting soldering between NbTi wires and Copper wires connecting the 4.2 K stage to room temperature, where there are also radio-frequency filters.
A further filtering stage is integrate on the Nb excitation coil, having a resistance of 40Ω obtained by deposition of a AuPd film. The resulting distributed RC filter has a cutting frequency in the GHz range. With this setup it is possible to control the rf SQUID state by an external flux and read it out by using a dc SQUID sensor coupled to the device through a superconductive flux transformer.

3.11 Experimental results for SQUID-based devices in the quantum regime

In this section the experimental study of decay from metastable states for Nb/AlO_x/Nb rf SQUID for temperatures in the milliKelvin region is reported.
A crossover temperature T_0 is defined in order to distinguish the thermal regime, $T>T_0$, where quantum effects are covered by thermal hopping, from quantum regime, $T<T_0$, where the main escape process is due to the Macroscopic Quantum Tunneling under the energy barrier and therefore the lifetime is no longer depending on temperature. For dissipative systems, T_0 is

expressed as [41]

$$T_0 = \frac{\hbar\omega_0}{2\pi k_B}\left[\left(1+\frac{1}{4Q^2}\right)^{1/2} - \frac{1}{2Q}\right] \tag{3.13}$$

where Q is the quality factor and ω_0 is the plasma frequency. In underdamped systems, that is Q$\gg$1, the expression of the crossover temperature can be simplified as follows:

$$T_0 = \frac{\hbar\omega_0}{2\pi k_B} \tag{3.14}$$

In quantum regime, the escape rate from the metastable states of an extremely underdamped system at T=0 K has been calculated by Caldeira and Leggett [42]. In their picture, dissipation is due to the interaction between the macroscopic quantum variable (in this case the phase of the Josephson junction) and the thermal bath, described by a system of harmonic oscillators with infinite degrees of freedom. Assuming a linear answer of the environment, the quantum escape rate has the following expression:

$$\Gamma_q = A_q\left(\frac{\omega_0}{2\pi}\right)\exp\left[-7.2\frac{\Delta U}{\hbar\omega_0}\left(1+\frac{0.87}{Q}\right)\right] \tag{3.15}$$

with

$$A_q = \left[120\pi\left(7.2\frac{\Delta U}{\hbar\omega_0}\right)\right]^{1/2} \tag{3.16}$$

Theoretical works extended this study to dissipative systems at finite temperature [43]. The resulting escape rate is given by

$$\Gamma_q^{GW} = A_q^{GW}\left(\frac{\omega_0}{2\pi}\right)\exp\left[-7.2\frac{\Delta U}{\hbar\omega_0}\left(1+\frac{0.87}{Q}\right)\right]\exp[C(T)] \tag{3.17}$$

with

$$A_q^{GW} = 12\sqrt{6\pi}(1+\frac{1.43}{Q}\left(\frac{\Delta U}{\hbar\omega_0}\right)^{1/2} \tag{3.18}$$

and

$$C(T) = \frac{36\pi}{Q}\frac{\Delta U}{\hbar\omega_0}\left(\frac{k_B T}{\hbar\omega_0}\right)^2 \tag{3.19}$$

represents a temperature depending correction, which is negligible in extremely low damping systems.
In configuration presented in Fig.3.13, the rf SQUID is coupled via a gradiometric flux transformer to a readout system, based on a dc SQUID sensor integrated on the same chip. Transitions between adjacent flux states of the rf SQUID have been measured as a function of the external flux Φ_x in order to record the switching probability distribution $P(\Phi_x)$. Data have been collected by standard time fly technique with $\Delta\tau_0$, the time interval corresponding to the change of a flux quantum in the rf SQUID, ranging between 1.52 ms and 1.74 ms (this time is controlled by changing the sweeping frequency to bias the rf SQUID). In Fig.3.17 the switching flux distribution $P(\Phi_x)$ of the rf SQUID, as a function of the external flux Φ_x, is reported at different temperatures ranging from 60mK to 4.2 K.

In Fig.3.17 it's possible to observe that for lower temperature, the shape of $P(\Phi_x)$ becomes gradually sharper, until the crossover temperature is reached. Then, below 250mK, the curves are overlapped. This saturation is due to the MQT phenomenon, which is an unavoidable enhancement of the escape process, even when thermal fluctuations are negligible. The crossover temperature can be better evaluated by looking at distribution width $\sigma = \sqrt{\langle\Phi_x^2\rangle - \langle\Phi_x\rangle^2}$ as a function of T. In thermal regime the distribution width is expected to scale as $T^{2/3}$ [44], while it has a constant value in quantum regime. The crossover temperature can be then defined by the intersection of the two curves, as shown in Fig.3.18.

The value of crossover temperature T_0 resulting from the experimental data is about 250 mK, so it is slightly higher than the expected one (about 200 mK). By fitting flux switching distributions in thermal regime with BHL theory [38], the values of the effective resistance R_{eff} is obtained. The re-

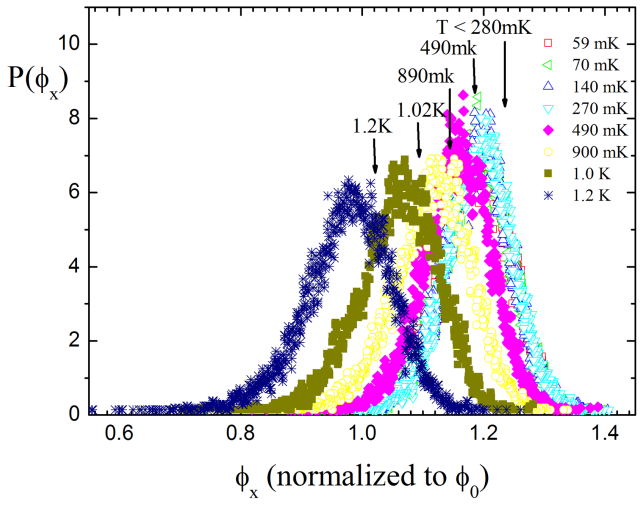

Figure 3.17: Sample in gradiometric configuration: experimental data for the switching flux distribution $P(\Phi_x)$ at different temperatures in the quantum regime. It's possible to observe that the shape of $P(\Phi_x)$ becomes gradually sharper, until the crossover temperature. Below the crossover temperature the curves are overlapped.

sulting value of about 1MΩ below T=1 K, confirms that the physical system is extremely underdamped, as defined by the BHL theory. The Q-factor for this rf SQUID device is of the order of 10^5 at $T \cong T_0$.

These preliminary characterizations have evidenced a low noise reading device with a good noise to signal ratio. The study of the decay process from the metastable flux states has allowed to assume a low dissipation level for these devices in the thermal regime, as well as to observe the MQT process in the quantum regime. These results confirm that this configuration is suitable to be used in the final experiment to be performed by using microwave. As future improvement it could be interesting to use a microwave pulse for a time Δt instead of a continuous signal.

Devices described here have been designed on the basis of first simulations, so that parameters used are not the optimal ones (that have been described

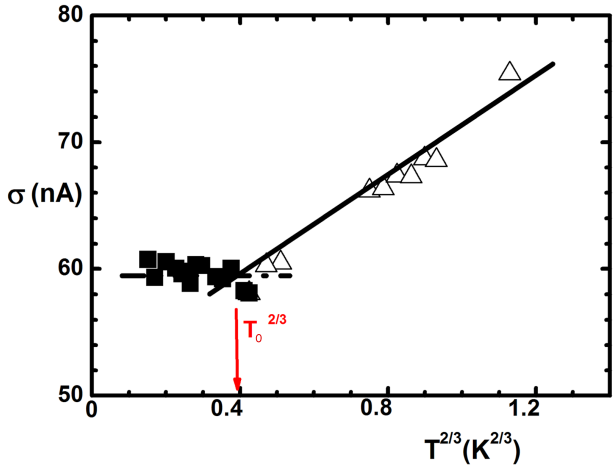

Figure 3.18: σ vs. $T^{2/3}$: theoretical predictions are obtained for R=1 MΩ and C=2.3 pF. Experimental extrapolation of the crossover temperature for the rf SQUID is T_0=250 mK.

in chapter 1). Work is in progress to realize devices in the parameter range in which the theory is expected to work.

Conclusions

This thesis presents theoretical and experimental research on Josephson devices that behave quantum mechanically. Results presented here describe the small viscosity limit in the problem of resonant quantum tunneling for a rf SQUID, whose parameters have been determined with independent measurements.

First a new theoretical approach has been developed in order to describe such phenomena and numerical simulations have been performed by the means of a C++ program.

In order to realize the experimental setup a detailed study on microwave filtering stage at low temperature, since components are not designed to wok at cryogenic temperature, has been realized. This study has allowed to realize the optimal setup for the experiment. Moreover a cryogenic insert has been especially designed in order to realize measurements in thermal regime and it has been tested by the means of a Josephson junction. Measurements in thermal and quantum regime have been performed on SQUID-based devices. Josephson devices have been designed and realized at ICIB-CNR of Naples. These experimental results provide a great deal of information in order to realize the final experiment on resonant macroscopic quantum tunneling in a SQUID-based device.

In fact results presented here can address some general topics in the study of macroscopic quantum phenomena and of possible applications to quantum

computing, since the studied device is a two level system and it can be considered as a quantum bit [45].
As future perspective it could be interesting to further study the theory on resonant macroscopic quantum tunneling by considering a different number of levels. Moreover it could be interesting also to perform a study by using another filtering stage, like a bandpass filter, in order to optimize the ratio S/N. Finally, as future improvement, it could be interesting to use a microwave pulse for a time Δt, in order to study also decoherence effects.

Appendix A

Josephson devices: the SQUIDs

A fundamental property of superconducting rings is that they can enclose magnetic flux only in multiples of a universal constant called the quantum flux Φ_0, defined as $\Phi_0 = h/2e$, where h is the Plank constant and e is the electron charge ($1.6 \cdot 10^{-19}$C). This physical effect can be exploited to produce an extraordinarily sensitive magnetic detector known as the Superconducting QUantum Interference Device, or SQUID. A SQUID is in essence a superconducting loop interrupted by one (rf SQUID) or two (dc SQUID) Josephson junctions. Several configuration are possible.

A.1 The rf SQUID

An rf SQUID is a superconductive loop interrupted by one Josephson junction. Quantum phase ϕ along the loop is a integer multiple [46] of the fundamental quantum flux Φ_0.
The relation between phase difference ϕ and flux Φ that is inside the loop gives the *fluxoid quantization* [17]:

$$\phi + 2\pi\Phi/\Phi_0 = 2\pi n \tag{A.1}$$

If we consider a superconductive loop having an inductance L, interrupted by a Josephson junction having a critical current I_c that is inside a magnetic field, then his behavior is expressed by the equation:

$$\vec{J} = n_s \frac{e}{m} \left[\hbar \vec{\nabla} \phi - 2 \frac{e}{c} \vec{A} \right] \tag{A.2}$$

where n_s is the number of superconductive electrons, m is the electron mass ($9.11 \cdot 10^{-31}$kg), c is the light speed ($3 \cdot 10^8$m/s), $\vec{A}$ is the *vector potential*, that depends on magnetic field $\vec{B}$ by the following relation $\vec{B} = \vec{\nabla} \times \vec{A}$.

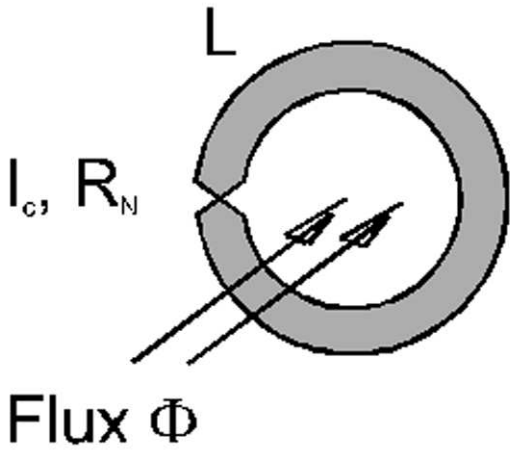

Figure A.1: A superconductive loop having an inductance L, interrupted by a Josephson junction having a critical current I_c.

It's possible to demonstrate [17] that the screening current circulating in the loop is:

$$I_s = -I_c \sin \left(2\pi \frac{\Phi}{\Phi_0} \right) \tag{A.3}$$

so that for an external flux Φ_{ex}, the total flux Φ in the loop is:

$$\Phi = \Phi_{ex} - \frac{\beta_L}{2\pi} \Phi_0 \sin \left(2\pi \frac{\Phi}{\Phi_0} \right) \tag{A.4}$$

where β_L is the *reduced inductance* defined as:

$$\beta_L = \frac{2\pi L I_c}{\Phi_0} \tag{A.5}$$

If we display Φ as a function of Φ_{ex}, there are two possible cases:

1. $\beta_L < 1$, Φ value is greater for greater values of Φ_{ex}
2. $\beta_L > 1$, curve is hysteretic

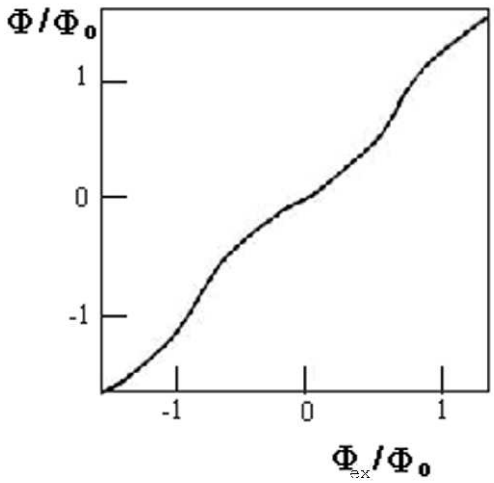

Figure A.2: Total flux Φ as a function of the external flux Φ_{ex} for a non-hysteretic device.

Now if we consider an hysteretic device and we suppose that there is no external flux, then the SQUID is in the zero flux state ($|0\rangle$). If now we apply a growing Φ_{ex}, the total flux Φ become greater, even if it grows slowly because of the field created by the superconductor, that generates an opposite flux LI_s, opposite to Φ_{ex}. This effect is much more evident for greater β_L values. When the screening current I_s is equal to I_c, that is for a flux value $\Phi_{ex,c}$ the junction makes a transition from fundamental state (V$\neq$0) to the resistive

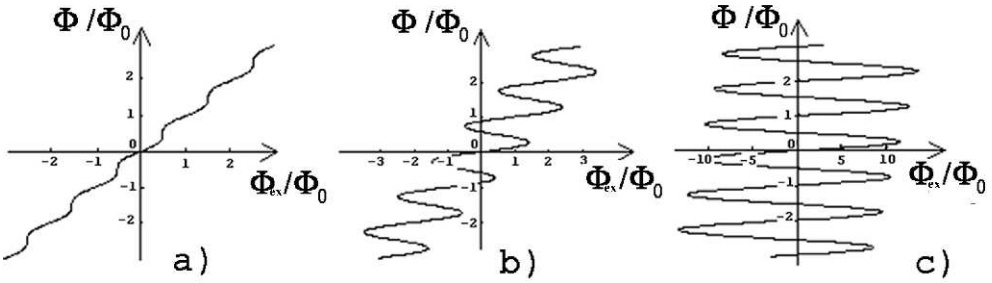

Figure A.3: Total flux Φ as a function of the external flux Φ_{ex} for a hysteretic device. a) $\beta_L = 1$; b) $\beta_L = 7.5$; c) $\beta_L = 70$

state (V=0) so that a quantum flux (Φ_0) can penetrate inside the loop. This let the SQUID to make a transition from the flux state $|0\rangle$ to the state $|1\rangle$ and the screening current I_s direction is inverted.

If we apply the Resistive Shunted Junction model [17] to the rf SQUID, we find that its dynamics is described by the equation

$$\Phi = \Phi_{ex} - LI_c \sin 2\pi \frac{\Phi}{\Phi_0} - LC\ddot{\Phi} - \frac{L}{R}\dot{\Phi} \tag{A.6}$$

After some calculations and by introducing the potential

$$U(\phi, \phi_{ex}) = U_0 \left(\beta_L \cos\phi + \frac{1}{2}(\phi - \phi_{ex})^2 \right) \tag{A.7}$$

where ϕ and ϕ_{ex} are respectively Φ and Φ_{ex} divided by $\frac{\Phi_0}{2}$ and normalized to $\frac{\Phi_0}{2\pi}$, β_L is defined by (A.5) and $U_0 = \frac{\Phi_0^2}{4\pi^2 L}$, the equation describing rf SQUID dynamics becomes:

$$C\ddot{\phi} + \frac{\dot{\phi}}{R} + \frac{\partial U(\phi, \phi_{ex})}{\partial \phi} = 0 \tag{A.8}$$

Eq.(A.8) is the equivalent of a particle having mass proportional to C and moving in a field described by the potential $U(\Phi, \Phi_{ex})$. This potential, for $\beta_L > 1$ presents different minima.

The shape and the barrier height (ΔU) [17, 8] for the potential depend on

Φ_{ex} value (Fig.A.4) and, for a fixed Φ_{ex}, they depend on β_L value.

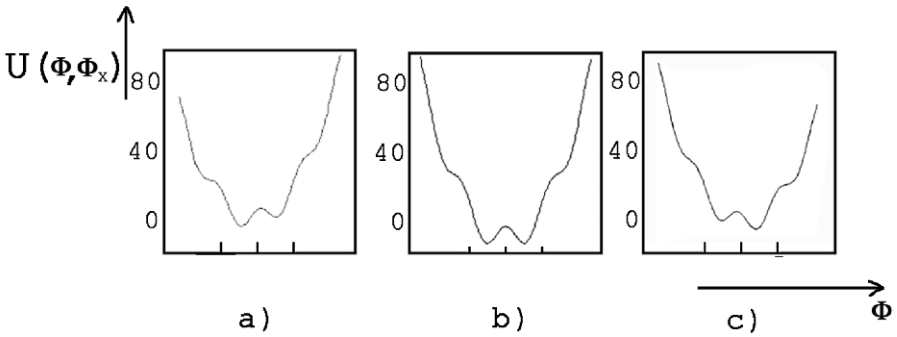

Figure A.4: Potential for a rf-SQUID, ϕ and ϕ_{ex} are obtained by dividing Φ and Φ_{ex} by $\Phi_0/2\pi$. a) $\Phi_{ex} = -1$; b) $\Phi_{ex} = 0$; c) $\Phi_{ex} = 1$.

A.2 The dc SQUID

The dc SQUID consists of two Josephson junctions coupled in parallel to a current source. This leads to a dependence of the effective Josephson energy of the double junction on the magnetic flux threading the SQUID loop. The circuit has two dynamical variables, superconducting phases, $\phi_{1,2}$ across the two Josephson junctions.

A.2.1 Readout of flux states by using a dc SQUID

In order to readout the flux states of an rf SQUID it's necessary to couple to a magnetic field detector.
SQUIDs actually function as magnetic flux-to-voltage transducers where the sensitivity is set by the magnetic flux quantum (Φ_0=2·10^{15}Wb). The output voltage of a SQUID is a periodic function of applied magnetic flux, going

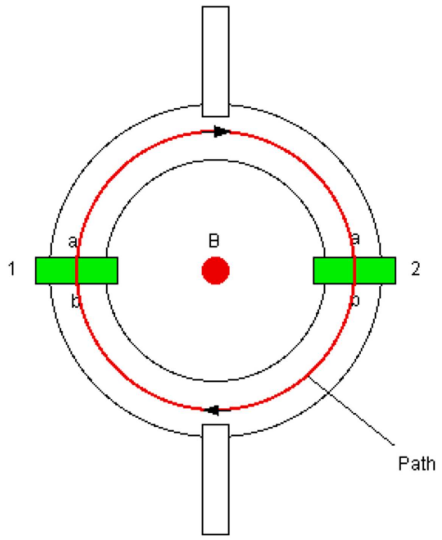

Figure A.5: Schematic representation for a dc SQUID

through one complete cycle for every flux quantum applied. Practical SQUID systems involve control electronics that interpolates between whole numbers of flux quanta and greatly enhances their ultimate sensitivity. SQUID sensitivity is finally limited by the intrinsic noise in the device.

So SQUIDs convert magnetic flux, which is hard to measure, into voltage, which is easy to measure and moreover they present an high sensitivity.Now if we suppose a constant current, known as a bias current, to pass through the SQUID. If the SQUID is symmetrical and the junctions are identical, the bias current will split equally, half on each side. A dc SQUID is generally represented schematically as shown in Fig.A.5.

A supercurrent will flow through the SQUID, as long as the total current flowing through it does not exceed the critical current of the Josephson junctions, which as we discussed earlier, have a lower critical current that the rest of the superconducting ring. The critical current is the maximum zeroresistance current which the SQUID can carry, or the current at which a

voltage across it develops.

When the two junctions in the SQUID are identical, the loop is symmetrical, and the applied field is zero, both junctions will develop a voltage at the same time. So the critical current of the SQUID is simply twice the critical current of one of its junctions.

If a tiny magnetic field is applied to the SQUID, the magnetic field wants to change the superconducting wave function. But the SQUID has to maintain an integral number of wavefunction cycles around the loop, so the superconducting loop opposes the applied magnetic field by generating a screening current I_s that creates a magnetic field equal but opposite to the applied field, effectively canceling out the net flux in the ring.

In order to understand the behavior of a dc SQUID it's necessary to obtain the I-Φ and I-V characteristics.

Here we consider the case the dc SQUID is biased with a current greater than the critical one ($\alpha = I_{bias}/I_c \sim 1.1$).

As we said before, we suppose the two junctions are equal, so that the critical currents are almost the same $I_1 \simeq I_2$. Then we can obtain the critical current I_c as a function of the external magnetic field $\vec{B}$, even if, for convenience we introduce the external flux

$$\Phi_{ex} = B_{\perp} O$$

where O is the area inside the superconducting loop.

First we suppose that the flux $\Phi_s = LI_s$ due to the screening current I_s can be neglected. The quantization rule implies:

$$\varphi_b^* - \varphi_a^* = \frac{2e}{\hbar} \oint \vec{A} \cdot d\vec{l} = 2\pi \frac{\Phi}{\Phi_0} \tag{A.9}$$

where $\Phi = \Phi_{ex} + LI_s$. The total current that flows through the SQUID is given by the sum of the currents that flow inside the single junctions:

$$\begin{aligned} I &= I\sin\varphi_a^* + I_1 \sin\varphi_b^* \\ &= I_1 \sin\varphi_a^* + I_1 \sin\left(\varphi_a^* + 2\pi\frac{\Phi_0}{\Phi_{ex}}\right) \\ &= 2I_1 \sin\left(\varphi_a^* + 2\pi\frac{\Phi_{ex}}{\Phi_0}\right)\cos\left(2\pi\frac{\Phi_{ex}}{\Phi_0}\right) \end{aligned} \tag{A.10}$$

So the maximum value for the critical current is:

$$I_c\left(\Phi_{ex}\right) = 2I_1\left|\cos\left(2\pi\frac{\Phi_{ex}}{\Phi_0}\right)\right| \tag{A.11}$$

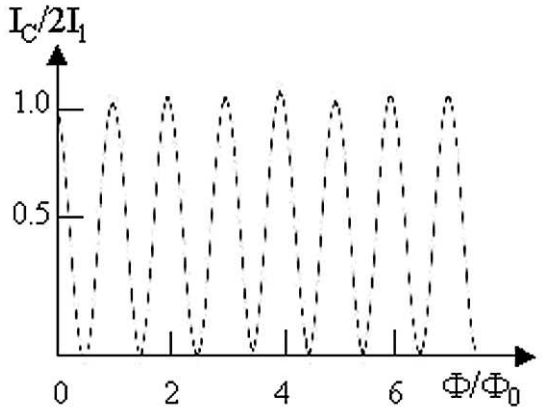

Figure A.6: Picture of critical current as a function of the external flux.

The critical current value becomes zero for flux values such that

$$\Phi_{ex} = \left(n + \frac{1}{2}\right)\Phi_0$$

Now if we consider devices with a really low impedance value, such that if we bias the ring with a current of the order of μA, inside the loop we can observe a flux comparable to Φ_0 and we can neglect LI_s no more.

If we don't neglect the self-inductance the flux Φ_s that flows inside the loop is equal to:

$$\Phi_s = \frac{1}{2} L I_1 \left(\sin\varphi_a^* - \sin\varphi_b^*\right) = \frac{L I_s}{2} \tag{A.12}$$

where

$$I_s = I_1 \left(\sin\varphi_a^* - \sin\varphi_b^*\right)$$

By using this expression we find

$$\begin{aligned} \frac{2\Phi_s}{L I_1} &= \sin\varphi_a^* - \sin\left(\varphi_a^* + 2\pi\frac{\Phi_{ex}+\Phi_s}{\Phi_0}\right) \\ &= -\sin\pi\left(\frac{\Phi_{ex}+\Phi_s}{\Phi_0}\right)\cos\left(\varphi_a^* + \pi\frac{\Phi_{ex}+\Phi_s}{\Phi_0}\right) \end{aligned} \tag{A.13}$$

and the total current here is:

$$\begin{aligned} I &= I_1\sin\varphi_a^* + I_1\sin\left(\varphi_a^* + 2\pi\frac{\Phi_{ex}+\Phi_s}{\Phi_0}\right) = \\ &= 2I_1\sin\left(\varphi_a^* + \pi\frac{\Phi_{ex}+\Phi_s}{\Phi_0}\right)\cos\left(\pi\frac{\Phi_{ex}+\Phi_s}{\Phi_0}\right) \end{aligned} \tag{A.14}$$

By eq.(A.13) and by eq.(A.14) it's possible to obtain the critical current as a function of the external magnetic field for different L values (Fig.A.7). As it's evident the critical current is a periodic function, with a period equal to Φ_0.

In order to obtain the I-V characteristic we have to consider also the normal current contribution. By using RSJ model it is possible to find:

$$I = I_1\left[\sin\varphi_a + \sin\varphi_b\right] + \frac{V}{R} \tag{A.15}$$

so we find that the eq.(A.15) becomes:

$$I = 2I_1\cos\pi\frac{\Phi+\Phi_s}{\Phi_0}\sin\varphi\left(t\right) + \frac{V\left(t\right)}{R} \tag{A.16}$$

From eq.(A.16) we obtain:

$$V\left(t\right) = RI - RI_1\cos\pi\frac{\Phi}{\Phi_0}\sin\varphi\left(t\right) = \frac{\hbar}{2e}\frac{\partial\varphi\left(t\right)}{\partial t} \tag{A.17}$$

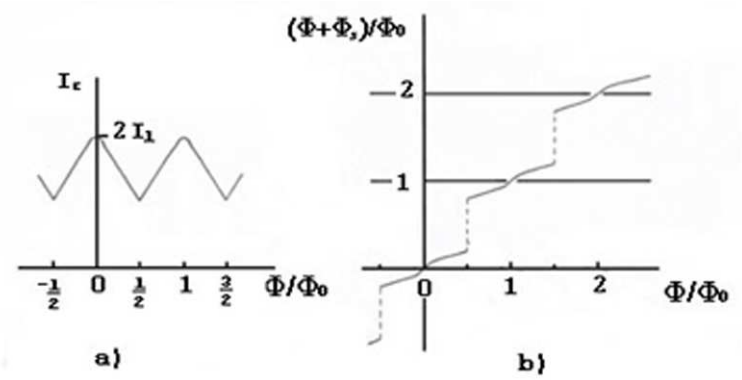

Figure A.7: (a) Picture of the critical current vs. the external magnetic flux icluding the effect due to the self-inducted Φ_s In the picture it is $\pi L I_1 = 5h/2e$. (b) Total flux inside the loop as a function of the external applied flux.

and

$$t = \frac{\hbar}{2e}\frac{1}{R}\int_{\varphi(0)}^{\varphi(t)} \frac{d\varphi}{I - I_1 \cos\pi\frac{\Phi}{\Phi_0}\sin\varphi\,(t)} \tag{A.18}$$

where the voltage V(t) is a periodic function of $\varphi(t)$ and the period is 2π; so V(t) is periodic in time with a period

$$T = \frac{\hbar}{2e}\frac{1}{R}\int_{0}^{2\pi} \frac{d\varphi}{I - I_1 \cos\pi\frac{\Phi}{\Phi_0}\sin\varphi\,(t)} \tag{A.19}$$

The mean value for V(t) is:

$$\bar{V} = \frac{1}{T}\int_0^T V\,(t)\,dt = \frac{1}{T}\frac{\hbar}{2e}\int_0^{2\pi}\frac{\partial\varphi}{\partial t}dt = \frac{1}{T}\frac{h}{2e} \tag{A.20}$$

and then:

$$\bar{V} = \frac{2\pi R}{\int_0^{2\pi}\frac{d\varphi}{I - I_1\cos\pi\frac{\Phi}{\Phi_0}\sin\varphi(t)}} \tag{A.21}$$

Solutions for this last equation are:

$$0 \leq I \leq I_c, \qquad \bar{V} = 0 \tag{A.22}$$

$$I > I_c, \qquad \bar{V} = R\sqrt{I^2 - I_c^2} \tag{A.23}$$

When $L \neq 0$ it's impossible to find an analytical expression for V(t), ma, anche in questo caso V but it is still a periodic function of Φ_{ex} with period Φ_0.

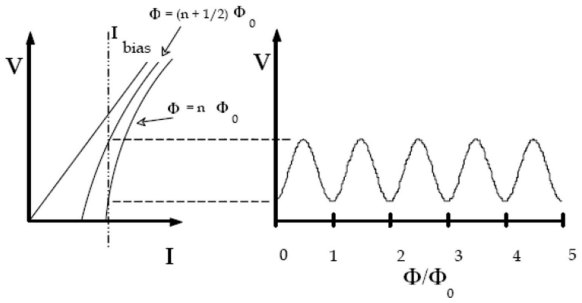

Figure A.8: a)Picture of I vs. V for a SQUID b)Picture of V-Φ characteristic for a dc SQUID

If we look at I-V curves for a dc SQUID (Fig.A.8a), for a fixed β_L^{dc} value $\left(\beta_L^{dc} = \frac{LI_c}{\Phi_0}\right)$, as a function of the external flux from $\Phi_{ex} = 0$ up to $\Phi_{ex} = \Phi_0/2$ it's possible to observe that the characteristic curve is always periodic but its value changes with growing current.
If we consider the critical current I_c as a function of the external flux Φ_{ex} for different β_L^{dc} values we find that I_c is periodic, with period equal to Φ_0. This curve is almost linear for $\Phi_{ex} = 0$ and $\Phi_{ex} = \Phi_0$, while it presents a cuspid for $\Phi_{ex} = \Phi_0/2$.
If we consider greater β_L^{dc} values, the modulation of critical current is really small, so that the SQUID cannot work as a good detector.

A.2.2 Linearity in dc SQUID

In presence of an external magnetic field the SQUID can be used as a flux-voltage transformer and as detector for little flux variations.
In fact, if we consider little variations in external magnetic flux, the SQUID voltage is linear and its expression is

$$\delta V = \delta\Phi \cdot V_\Phi \tag{A.24}$$

where V_Φ is the *responsivity* and it's defined as

$$V_\Phi = \left| \left(\frac{\partial V}{\partial \Phi} \right)_I \right|$$

For $\Phi = \Phi_0/4$ the responsivity is such that the voltage variation corresponding to external flux variation is maximum.
Moreover by measuring δV it's possible to evaluate the magnetic flux value and, by using eq.(A.25), it's also possible to calculate the corresponding magnetic field

$$B = \frac{\delta\Phi}{A_{eff}} \tag{A.25}$$

where A_{eff} is the device "effective area".

A.3 Dissipation mechanisms for Josephson devices

Finally there are some important parameters in order to describe different aspects of dissipation mechanism. First there is the resistance of the *normal state* (R_N), that is the resistance of the junction when the two bulk metals on the two sides are above their transition temperature T_0.
Then there is the zero bias subgap resistance R_{qp} due to the presence of thermally activated quasiparticles.

Finally, there's the R_{eff} is the *effective resistance*, that can be several orders of magnitude higher than R_N. This parameter, as long as the junction dissipation is dominated by an intrinsic mechanism, depends exponentially on the temperature T, [17]

$$R_{eff} \cong R_0 \exp(\Delta / K_B T) \tag{A.26}$$

where Δ is the superconducting gap and K_B is the Boltzmann constant. As a consequence, at low temperatures, we have been able to obtain an extremely low dissipation level (R_{eff} >40kΩ).
The effective resistance of a Josephson tunnel junction is unambiguously correlated [47, 48, 49] to the zero bias subgap resistance R_{qp} due to the presence of thermally activated quasiparticles. The evidence of this correlation is quite convincing with no use of free fitting parameters. Moreover, the resistance depends exponentially on the temperature. Therefore, decreasing the temperature we have been able to obtain an extremely low dissipation level.
The R_{qp} generally differs from the normal junction resistance R_N and strongly depends on temperature and applied voltage.

Published papers

1. P.Silvestrini, R.Russo, V.Corato, B.Ruggiero, C.Granata, S.Rombetto, M.Russo, M.Cirillo, A.Trombettoni, P.Sodano *Topology-Induced Critical Current Enhancement in Josephson Networks*, cond-mat/0512478.

2. Yu.N.Ovchinnikov, S.Rombetto,B.Ruggiero, V.Corato, P.Silvestrini, *Resonance phenomena in macroscopic quantum tunneling: Small-viscosity limit*, quant-ph/0611255.

3. B.Ruggiero, C.Granata, A.Vettoliere, S. Rombetto, R. Russo, M. Russo, V. Corato, and P. Silvestrini, *rf SQUID system as tunable flux qubit* Physics Letters A, Volume 356, Issue 6, (2006), 451-456.

4. C Granata, A Vettoliere, M Lisitskiy, S Rombetto, M Russo, B Ruggiero, V Corato, R Russo and P Silvestrini *Vertical Josephson Interferometer for Tunable Flux Qubit*, **Journal of Physics: Conference Series** 43 (2006), 14051408.

5. S. Rombetto, V.Corato, Yu.N. Ovchinnikov, B.Ruggiero and P.Silvestrini, *Resonance Phenomena in the Macroscopic Quantum Tunnelling* **Journal of Physics: Conference Series** 43 (2006), 11951198.

6. Yu.N.Ovchinnikov, P.Silvestrini, V.Corato, **S.Rombetto**, *Resonance phenomena in macroscopic quantum tunnelling for an rf-SQUID*, **Phys. Rev. B**71, 024529 (2005).

7. V.Corato, **S.Rombetto**, C.Granata, E.Esposito, L.Longobardi, R.Russo, B.Ruggiero and P.Silvestrini, *Quantum behaviour of underdamped Josephson devices*, **Phys. Rev. B**70, 172502 (2004).

8. V.Corato, **S.Rombetto**, P.Silvestrini, C.Granata, R.Russo and B.Ruggiero, *Observation of Macroscopic Quantum Tunnelling in a rf SQUID system*, **Supercond. Sci. Technol. 17**(2004) S385-388.

9. B. Ruggiero, V. Corato, C. Granata, **S.Rombetto** and P. Silvestrini, *Measurement of the effective dissipation in an rf SQUID system*, **Phys. Rev. B**67, 132504 (2003)

10. C.Granata, V.Corato, L.Longobardi, **S.Rombetto**, M.Russo, B.Ruggiero, and P.Silvestrini, *Macroscopic Quantum Device Based on a rf SQUID System*, **IEEE Trans. on Appl. Supercond.** Volume 13, Issue 2, Part 1, June 2003 Page(s):1001-1004.

11. V.Corato, C.Granata, L.Longobardi, **S.Rombetto**, M.Russo, B.Ruggiero, L.Stodolsky, J.Wosiek, and P.Silvestrini, *SQUID system in view of macroscopic quantum coherence and adiabatic quantum gates*, in **"Quantum Computing and Quantum Bits in Mesoscopic Systems"**, A. J. Leggett, B. Ruggiero, and P. Silvestrini eds. Kluwer Academic Plenum Publishers, NY USA, (Dicembre 2003).

12. L.Longobardi, V.Corato, C.Granata, S.Rombetto, M.Russo, B.Ruggiero, and P.Silvestrini, *Rf-SQUID based device for MQC*, **Intern. J. of Modern Physics B, Vol.17**, 762-767 (2003).

13. L. Longobardi, V. Corato, C. Granata, **S.Rombetto**, M. Russo, B. Ruggiero, and P. Silvestrini, RF SQUID based device for MQC, in "High Temperature Transition Superconductors", G. Maritato, R. Vaglio, eds, Word Scientific Singapore (2003)

Bibliography

[1] P. Silvestrini, Y. Ovchinnikov, and B. Ruggiero, "Resonant macroscopic quantum tunneling in squid systems," *Phys. Rev. B*, vol. 54, p. 1246, 1996.

[2] Y. Ovchinnikov, P.Silvestrini, V. Corato, and S. Rombetto, "Resonance phenomena in macroscopic quantum tunneling for an rf squid," *Phys. Rev. B*, vol. 71, p. 024529, 2005.

[3] S.Rombetto, V.Corato, Yu.N.Ovchinnikov, B.Ruggiero, and P.Silvestrini, "Resonance phenomena in the macroscopic quantum tunnelling," *Journal of Physics: Conference Series*, vol. 43, pp. 1195–1198, 2006.

[4] U. Fano, "Description of states in quantum mechanics by density matrix and operator techniques," *Rev. of Mod. Phys.*, vol. 29, p. 74, 1957.

[5] A. Larkin and Y. Ovchinnikov *Sov. Phys. JETP*, vol. 64, p. 185, 1986.

[6] L. Landau and L. Lifshitz, *Quantum Mechanics: non-relativistic theory.* Butterworth-Heinemann, 1981.

[7] S. Han, R. Rouse, and J. Lukens, "Observation of cascaded two-photon-induced transitions between fluxoid states of a squid," *Phys. Rev. Lett.*, vol. 84, p. 1300, 2000.

[8] J. Friedman, V. Patel, S. T. W. Chen, and J. Lukens, "Quantum superposition of distinct macroscopic states," *Nature (London)*, vol. 406, p. 43, 2000.

[9] J. B. Majer, F. G. Paauw, A. J. ter Haar, C. J. P. Harmans, and J. E. Mooij *Phys. Rev. Lett.*, vol. 94, p. 090501, 2005.

[10] J. Claudon, F. Balestro, F. W. J. Hekking, and O. Buisson, "Coherent oscillations in a superconducting multilevel quantum system,"

[11] Y. N. Ovchinnikov and A. Schmid, "Resonance phenomena in the current-voltage characteristic of a josephson junction," *Phys. Rev. B*, vol. 50, p. 6332, 1994.

[12] P. Silvestrini, B. Ruggiero, and A.Barone *J. Supercond.*, vol. 5, p. 481, 1992.

[13] R. Simmonds, L. K.M., D. Hite, S. Nam, D. Pappas, and J. Martinis, "Decoherence in josephson phase qubits from junction resonators," *Phys. Rev. Lett.*, vol. 93, p. 077003, 2004.

[14] B. R. edited by A. J. Leggett and P. Silvestrini, *Quantum Computing and Quantum Bits in Mesoscopic Systems.* Kluwer Academic/Plenum Publishers NY USA, 2004.

[15] A. Larkin and Y. Ovchinnikov *J. of Low. Temp. Phys.*, vol. 63, p. 317, 1986.

[16] R. Rouse, S. Han, and J. Lukens *Phys.Rev.Lett.*, vol. 75, p. 1614, 1995.

[17] A. Barone and G. Paterno, *Physics and applications of the Josephson effect.* New York: Wiley, 1982.

[18] P. Silvestrini, V. G. Palmieri, B. Ruggiero, and M.Russo, "Observation of energy levels quantization in underdamped josephson junctions above the classical-quantum regime crossover temperature," *Phys. Rev. Lett.*, vol. 79, p. 3046, 1997.

[19] Y. Ovchinnikov, S. Rombetto, B.Ruggiero, V. Corato, and P.Silvestrini, "Resonance phenomena in macroscopic quantum tunneling: the small viscosity limit," *quant-ph/0611255*, 2006.

[20] A. Larkin and Y. Ovchinnikov, "Resonance phenomena in the current-voltage characteristic of a josephson junction," *Phys. Rev. B*, vol. 50, p. 6332, 1994.

[21] I. Siddiqi, R. Vijayand, F. Pierreand, C. M. Wilsonandand, M. Metcalfeandand, C. Rigettiand, L. Frunzio, and M. H. Devoret, "Rf-driven josephson bifurcation amplifier for quantum measurement," *Phys. Rev. Lett.*, vol. 93, p. 207002, 2004.

[22] I. Siddiqi, R. Vijay, F. Pierre, C. M. Wilson, L. Frunzio, M. Metcalfe, C. Rigetti, R. J. Schoelkopf, and M. H. Devoret, "Direct observation of dynamical bifurcation between two driven oscillation states of a josephson junction," *Phys. Rev. Lett.*, vol. 94, p. 027005, 2005.

[23] P. A. Rizzi, *Microwave Engeneering - Passive Circuits.* Prentice Hall, Englewood Cliffs, New Jersey 07632, 1988.

[24] S. Ramo, J. R. Whinnery, and T. V. Duzer, *Fields and Waves in Communication Electronics, 2nd ed.* Wiley, 1984.

[25] A. Zorin, "The thermocoax cable as the microwave frequency filter for single electron circuits," *Rev. Sci. Instrum.*, vol. 66, p. 4296, 1995.

[26] B.Ruggiero, C.Granata, E.Esposito, M.Russo, and P. Silvestrini *Appl. Phys. Lett.*, vol. 75, 1999.

[27] E. Esposito, C. Granata, B. Ruggiero, M. Russo, L. Serio, and P. Silvestrini, "Filtering systems to reduce the external noise in macroscopic quantum tunneling experiments," *CNR-IC Internal Report*, 1999.

[28] T. A. Fulton and L. N. Dunkleberger, "Lifetime of the zero-voltage state in josephson tunnel junctions," *Phys. Rev. B*, vol. 9, p. 4760, 1974.

[29] P. Silvestrini, O. Liengme, and K. E. Gray, "Current distributions of thermal switching in extremely underdamped josephson junctions," *Phys. Rev. B*, vol. 37, p. 1525, 1988.

[30] P.Silvestrini, S.Pagano, and R. Cristiano, "Effect of dissipation on thermal activation in an underdamped josephson junction: First evidence of a transition between different damping regimes," *Phys. Rev. Lett.*, vol. 60, p. 844, 1988.

[31] M.Devoret, J.M.Martinis, D.Esteve, and J.Clarke, "Measurements of macroscopic quantum tunneling out from the zero-voltage state of a current-biased josephson junction," *Phys. Rev. Lett.*, vol. 55, no. 18, p. 1908, 1985.

[32] M.Devoret, J.M.Martinis, and J.Clarke, "Measurements of macroscopic quantum tunneling out from the zero-voltage state of a current-biased josephson junction," *Phys. Rev. Lett.*, vol. 55, no. 18, p. 1908, 1985.

[33] M.H.Devoret, D.Esteve, J.M.Martinis, A.Cleland, and J.Clarke, "Resonant activation of a brownian particle out of a potential well: Microwave-ehnanced escape from the zero-v voltage state of a josephson junction," *Phys. Rev. B*, vol. 36, no. 1, p. 58, 1987.

[34] C. Granata, V. Corato, A. Monaco, B. Ruggiero, M. Russo, and P. Silvestrini *Appl. Phys. Lett.*, vol. 79, p. 1145, 2001.

[35] B.Ruggiero, V. Corato, C. Granata, L. Longobardi, S. Rombetto, and P. Silvestrini, "Measurement of the effective dissipation in an rf squid system," *Phys. Rev. B*, vol. 67, p. 132504, 2003.

[36] B.Ruggiero, C.Granata, A.Vettoliere, S.Rombetto, R.Russo, M.Russo, V.Corato, and P. Silvestrini, "rf squid system as tunable flux qubit," *Phys. Letters A*, vol. 356, pp. 451–456, 2006.

[37] V.Corato, C.Granata, S.Rombetto, B.Ruggiero, M. Russo, R. Russo, P.Silvestrini, and A. Vettoliere, "Tunable josephson devices for quantum computation," *IEEE Trans. On Appl. Supercond.*, p. *(in press)*, 2006.

[38] M. Buttiker, E. P. Harris, and R. Landauer, "Thermal activation in extremely underdamped josephson-junction circuits," *Phys. Rev. B*, vol. 28, p. 1268, 1983.

[39] A. Kramers *Physica*, vol. 7, p. 284, 1940.

[40] R. Dolata, H. Scherer, A. B. Zorin, and J. Niemeyer *Appl. Phys. Lett.*, vol. 80, p. 2776, 2002.

[41] A. I. Larkin and Y. N. Ovchinnikov, *Quantum Tunneling in Condensed Media*. Elsevier Science Publishers, 1992.

[42] A. Caldeira and A. Leggett, "Influence of dissipation on quantum tunneling in macroscopic systems," *Phys. Rev. Lett.*, vol. 46, p. 211, 1981.

[43] U. Weiss, *Quantum Dissipative Systems*. World Scientific, Singapore, 1999.

[44] J. Kurkijarvi, "Intrinsic fluctuations in a superconducting ring closed with a josephson junction," *Phys. Rev. B*, vol. 6, p. 832, 1972.

[45] M. Nielsen and I. Chuang, *Quantum computation and quantum information*. Cambridge University Press.

[46] F. London, *Macroscopic theory of superfluid helium, Superfluids vol.II*. Dover Edition, New York, 1964.

[47] R. Cristiano, L. Frunzio, C. Nappi, M. G. Castellano, G. Torrioli, and C. Cosmelli, "The effective dissipation in nb/alo x/nb josephson tunnel junctions by return current measurements," *J. Appl. Phys.*, vol. 81, p. 7418, 1997.

[48] S.Washburn, R.A.Webb, R.F.Voss, and S.M.Faris, "Effect of dissipation and temperature on macroscopic quantum tunneling," *Phys. Rev. Lett.*, vol. 54, no. 25, p. 2712, 1985.

[49] B.Ruggiero, C.Granata, V. Palmieri, M.Russo, A.Esposito, and P.Silvestrini, "Supercurrent decay in extremely underdamped josephson junctions," *Phys. Rev. B*, vol. 57, p. 134, 1998.

List of Figures

List of Tables